This is the peer-reviewed, final accepted version for American Mineralogist, published by the Mineralogical Society of America.
The published version is subject to change. Cite as Authors (Year) Title. American Mineralogist, in press.
DOI: https://doi.org/10.2138/am-2021-7888. http://www.minsocam.org/

Revision 2 Word Count: 10975

Transformation of Fe-bearing minerals from Dongsheng sandstone-type uranium deposit, Ordos Basin, north-central China: Implications for ore genesis

Liang Yue[1,2,3], Yangquan Jiao[1,2,*], Mostafa Fayek[3], Liqun Wu[1,2], Hui Rong[1,2], Huili Xie[4]

[1] *Key Laboratory of Tectonics and Petroleum Resources (China University of Geosciences), Ministry of Education, Wuhan 430074, China*

[2] *School of Earth Resources, China University of Geosciences, Wuhan 430074, China*

[3] *Department of Geological Sciences, University of Manitoba, Winnipeg R3T 2N2, Canada*

[4] *CNNC Beijing Research Institute of Uranium Geology, Beijing 100029, China*

Abstract

Iron-bearing mineral assemblages and their distribution patterns directly reflect the redox environment in sediments, which plays a decisive role in the migration and precipitation of U. The Dongsheng sandstone-type U deposit hosted in fluvial and/or deltaic sandstones of the lower member of the Middle Jurassic Zhiluo Formation in the northeastern Ordos Basin has experienced multiple fluid events that impacted the redox conditions. Highly enriched in barren grey sandstones, pre-ore U (U_{mean} = 12.05 ppm) associated with Fe-Ti oxides, clay minerals and organic matter is likely one of the key sources of U for the mineralization. Different contents of Fe-bearing minerals including biotite, Fe-Ti oxides, pyrite, hematite, goethite, and chlorite that were formed or altered under different redox conditions, resulted in sandstone units with distinct colors. The red sandstone is hematite-rich, indicating a highly oxidizing environment. The green sandstone is chlorite-rich

*Corresponding author.
Email address: yqjiao@cug.edu.cn.

and formed because of reducing hydrocarbon-rich fluids that overprinted the hematite-rich sandstone. The barren and mineralized grey sandstones consist of pyrite (with a higher content in mineralized sandstones), Fe-Ti oxide minerals, and carbonaceous debris, which are indicators of a reducing environment. Based on the paragenetic relationship and sulfur isotopic compositions of ore-stage pyrite, bacterial sulfate reduction was responsible for the formation of framboidal pyrite ($\delta^{34}S$ = -31.2 to -3.8‰), and the sulfur of this pyrite mainly came from the oxidation of pre-ore pyrite ($\delta^{34}S$ = -19.1 to +20.3‰). Euhedral and cement pyrite overprinting framboids were produced via Ostwald ripening with $\delta^{34}S$ values ranging from -56.9 to -34.3‰, lower than any values of framboidal pyrite. Therefore, these mineralogical and geochemical characteristics of the Dongsheng deposit suggest U mineralization involved both biogenic and abiogenic redox processes.

Keywords: Pyrite, $\delta^{34}S$, Fe-bearing minerals, alteration, sandstone-type U deposit, Ordos Basin

Introduction

Large-scale sandstone-type U deposits in China are mainly distributed in sedimentary basins generally parallel to the Central Asian Orogenic Belt (Chen 2002; Huang and Huang 2005; Zhang et al. 2010; Jiao et al. 2015; Zhu et al. 2018). The Dongsheng U deposit, located at the southeastern margin of the Central Asia Uraniferous Province (CAUP; OECD-NEA, IAEA 2010), has experienced multiple low-temperature fluid events responsible for multi-stage mobilization and fixation of U (e.g., Miao et al. 2010; Zhang et al. 2019). Having simple fluid histories quite different from the complex fluid history in the Dongsheng deposit, the ore-forming process of

other sandstone-type U deposits in the CAUP (e.g., the Bayinwula deposit in the Erlian basin, Bonnetti et al. 2015; the Kuji'ertai and Mengqiguer deposits in the Yili basin, Zhang and Liu 2019), is similar to the roll front reported by Shawe and Granger (1965) and Warren (1971). However, the genesis of the Dongsheng deposit remains controversial, with two models proposed including biogenic processes due to confirmed existence of bacteria (Cai et al. 2007a, 2007b; Jiang et al. 2012) and hydrothermal mineralization (Xiao et al. 2004; Zhang et al. 2017).

It has been widely accepted that U mineralization of sandstone-type deposits occurs during infiltration of the low-temperature surface-derived oxygenated groundwater into permeable sandstones. Containing abundant intrinsic or extrinsic reductants (e.g., organic matter, H_2S and FeS_2; Granger and Warren 1969; Goldhaber et al. 1983; Jiao et al. 2018a; Hough et al. 2019; Bonnetti et al. 2020), those permeable sandstones are confined by non- to semi-permeable aquitards (e.g., coal seams and mudstones). In this process, soluble U (VI) is reduced to insoluble U (IV). Additionally, iron is a redox-sensitive element with a high abundance in natural environments (e.g., Soliman and Goresy 2012; Mahoney et al. 2019). The mobilization, migration and fixation of U are often accompanied by variations in the existing forms of Fe species (i.e., different Fe-bearing minerals; Reynolds and Goldhaber 1978; Bonnetti et al. 2015; Rong et al. 2016). Therefore, the distribution and alteration characteristics of Fe-bearing minerals, in turn, reveal the geochemical zoning of the host sandstones, thus helping to decipher the genesis of U deposits. The changes of redox environment can also be indicated by the distribution characteristics of organic materials (e.g., total organic carbon; Spirakis 1996). It is known that

organic materials can not only provide energy for microbial activities involved in the alteration of Fe-bearing minerals (Reynolds et al. 1982; Reynolds and Goldhaber 1983), but also adsorb U under reducing conditions (Douglas et al. 2011; Zhang et al. 2020). Although the metallogenic model for the Dongsheng U deposit is well established, and in outcrops, U anomalies mainly associated with carbonaceous debris (CD) in the yellow sandstone have been reported by Jiao et al. (2018b) and Zhang et al. (2019a), the distribution characteristics of Fe-bearing minerals in different geochemical zones of host sandstones, especially the alteration of these minerals, are poorly understood.

The purpose of this paper is to characterize the role of Fe-bearing minerals in the mobilization and fixation of U in the Dongsheng deposit in the Ordos Basin. Mineralogical, chemical, and sulfur isotopic data are used to evaluate their alteration processes and to characterize the genetic link between Fe-bearing and U-bearing minerals. Here, we propose that biogenic activities and the following abiogenic processes were involved in the U mineralization in the Dongsheng deposit, thereby providing a better understanding for the genesis of U deposits in northern China.

Geological background

The Ordos Basin

The Ordos Basin is a rectangular, NNE-trending basin located in north-central China (Fig. 1a), covering an approximate area of 250, 000 km^2 (Deng et al. 2005). Based on the current tectonic configuration, the basin can be divided into six structural domains (Fig. 1a): the Yimeng uplift, the Western fault-folded zone, the Tianhuan depression, the Shanbei slope, the Jinxi folded zone, and

81 the Weibei uplift (Guo and Jiao 2002).

82 The Ordos Basin developed during five main stages (Sun et al. 1985; Li et al. 1992; Zhang et al.
83 1995; Zhao et al. 1996; Zhang and Liao 2006; Jiao et al. 2015; Peng et al. 2019): (1) an aulacogen
84 stage characterized by Mesoproterozoic to Neoproterozoic metamorphic rocks, including phyllites,
85 marbles, greenschists and metamorphosed volcanic rocks (Zhang et al. 1980; Jia et al. 1997; Yang
86 et al. 2005); (2) an epicontinental sea stage marked by early Paleozoic limestone, evaporite and
87 gas-rich carbonate rocks of neritic platform facies (Sun et al. 1986; Zhai et al. 2002); (3) a
88 depression stage characterized by late Paleozoic to early Mesozoic coal, limestone, and gas- and
89 oil-bearing sandstone and mudstone (Li et al. 1995; Liu and Yang 2000); (4) an independent intra-
90 continental basin stage characterized by deposition of middle to late Mesozoic sedimentary units
91 dominated by fluvial, deltaic and lacustrine environments, and containing various energy resources
92 including (from oldest to youngest in Jurassic sediments) oil in the Fuxian Formation, oil and coal
93 in the Yan'an Formation, and U in the Zhiluo Formation (Qu et al. 2003; Yang et al. 2005; Zhang
94 et al. 2006; Cai et al. 2007a); and (5) a fault depression stage characterized by generation of a
95 series of grabens in the Cenozoic around the basin, thereby destroying the integrity of the basin
96 (Zhao, Z.Y. 1990; Zhao, M.W., et al. 1996; He 2003).

97 Several NW- and NNE-trending faults are developed in the northern Ordos Basin (Fig. S1; Han
98 et al. 2008), some of which cut through the early Paleozoic to middle Mesozoic sediments (Chen
99 et al. 2005; Deng et al. 2005; Liu et al. 2009). Based on thermal and tectonic history analyses
100 reported by Zhao et al. (1996), the Ordos Basin has undergone a short-lived thermal event in

Middle Jurassic (170-160 Ma), and this event was attributed to the subsurface magmatic intrusion related to the early Yanshanian movement and resulted in the initial formation of hydrocarbons in Paleozoic sediments and migration from them. In addition, the differential uplift and erosion between the eastern and western parts of the basin since 23 Ma led to a regional upward migration of hydrocarbons (Zhao et al. 1996; Zhang et al. 2018), which was indicated by carbon isotope values and fluid inclusion compositions in calcite cement in the Zhiluo Formation (e.g., Cai et al. 2007b).

The Dongsheng uranium deposit

The Dongsheng U deposit, located in the northeastern Ordos Basin (Fig. 1a), is hosted in the sandstone of the Middle Jurassic Zhiluo Formation (J_2z) deposited as climate changed from semi-humid to semi-arid (Miao et al. 2010; Sun et al. 2017; Jiao et al. 2018a). The Zhiluo Formation unconformably overlying the Middle Jurassic coal-bearing strata of the Yan'an Formation (J_2y) is composed of lowstand, transgressive and highstand systems tracts, and the lowstand systems tract consists of two parasequence sets (Jiao et al. 2005a, 2005b). The lower parasequence set (J_2z^{1-1}) originated from a braided river (delta) is the primary ore-bearing stratum. The upper parasequence set (J_2z^{1-2}) originated from a meandering river (delta) is the secondary ore-bearing stratum. Two main tabular orebodies have been delineated based on their different horizons (i.e., J_2z^{1-1}, J_2z^{1-2}; Fig. 1b), showing 0.5 to 5 m in thickness and dip direction of northwest-southeast with a burial depth decreasing from 800 to 100 m. The orebodies extend for over 100 km along the redox front and are a few hundred meters to a kilometer wide (Peng et al. 2019). The inferred and indicated

resources total more than 50 kt at 0.03 to 0.1% U (Akhtar et al. 2017; Zhu et al. 2018; Peng et al. 2019). The U mineralization is mainly hosted in coarse to medium-grained sandstones in the middle and upper parts of the fluvial facies (Figs. 1 and 2). Uranium minerals mainly occur as coffinite and uraninite and are associated with CD and pyrite (Jiao et al. 2018a; Yue et al. 2019).

Four facies displaying different colors are identified in the deposit: red sandstone (Figs. 1b-1d and 2a), green sandstone (Figs. 1b-1d and 2b-2c), grey sandstone (Figs. 1b-1d and 2d-2h) and yellow sandstone (Fig. 1c and 1d), classified into: (1) oxidized zone, consisting of red, green and yellow sandstones, (2) mineralized zone hosted by grey sandstones, and (3) reduced zone with barren grey sandstones (Fig. 2). Clay minerals are composed of an assemblage of smectite-kaolinite-chlorite-illite in the sandbodies, with a higher content of chlorite in the green sandstone and a higher content of kaolinite in the mineralized grey sandstone (e.g., Zhang et al. 2019).

Sampling and analytical methods

A total of 109 sandstone samples from three regional stratigraphic drill holes (DSA, DSB and DSC) and three drill holes through the Dongsheng U deposit (DS1, DS2 and DS3), and 21 outcrop sandstone samples from Shenshangou area were collected. Detailed sample locations and descriptions are shown in Figures S1-S3 and Tables S1-S2.

Ninety-nine drill core samples (27 red, 33 green and 39 barren grey sandstone samples; Fig. S2) combined with 7 yellow outcrop sandstone samples (Fig. S3) were analyzed for their U and Th contents (Table S1). Three drill holes DSA-DSC were used as a reference to determine the petrographic, mineralogical and geochemical characteristics of the host sandstone before U

141 mineralization. Thirty-five different colored samples (7 red, 7 green, 7 mineralized grey, 7 barren
142 grey and 7 yellow sandstone samples; Figs. S2 and S3; Table S2) were analyzed for redox-sensitive
143 indicators (i.e., Fe^{3+}, Fe^{2+}, S^{2-}, S_{total}, TOC, ΔEh and pH). The ΔEh and pH of the sandstones were
144 tested with international standards, i.e., ISO11271:2002 and ISO10390:2005, respectively. The
145 analyses of U, Th and redox-sensitive indicators were carried out, by using a HD3025 laser
146 analyzer for U (relative standard deviation (RSD) = 4.18%), a modal 721 spectrophotometer for
147 Th (RSD = 2.60%), a 5mL acid burette for Fe^{3+} (RSD = 0.10 to 1.24%), Fe^{2+} (RSD = 0.22 to 1.35%)
148 and TOC (RSD = 0.10 to 1.30%), a HCS-140 high frequency infrared ray carbon-sulphur analyzer
149 for S_{total} (RSD = 0.24 to 1.65%), a ESJ200-4 electronic balance for S^{2-} (RSD = 0.18 to 1.40%), an
150 electronic potentiometer for ΔEh (RSD = 0.30 to 1.50%) and a PHS-3C acidimeter for pH (RSD
151 = 0.12 to 1.50%) at the Analyses and Testing Center in No.208 Geological Party, China Nuclear
152 Geology, Chinese National Nuclear Corporation, Baotou, China.
153 Thirty-five samples (Table S2) were prepared as polished thin sections and characterized, by
154 using a Nikon ME600POL optical microscope and a Zeiss EVO LS 15 scanning electron
155 microscope (SEM) at the Key Laboratory of Tectonics and Petroleum Resources Ministry of
156 Education, China University of Geosciences, Wuhan. Observations were focused on the U-bearing
157 and Fe-bearing minerals to determine their textural and paragenetic relationships. Electron probe
158 microanalysis (EPMA) was chosen to quantify the chemistry of U-bearing and Fe-bearing minerals
159 at the University of Manitoba, Winnipeg, Canada, by using a Cameca SX100 universal electron
160 probe microanalyzer. The EPMA beam size was adjusted between 1 and 10 μm, which depended

on the detail required. The acceleration voltage was 15 kV and the current was 20 nA.

Twenty-two thin sections (5 red, 5 green, 5 mineralized grey, 2 barren grey and 5 yellow sandstone samples; Table S2) were selected for pyrite sectional area counts within a 2 cm^2 area by SEM. The percentage area covered by pyrite grains in the photomicrographs is measured, by using the software named Image-Pro Plus 6.0. We tried to approximate the average content of pyrite in sandstones using the ratio of cross-sectional area of pyrite to 2 cm^2 in thin sections (Fig. S4).

In order to preserve isotopic values in their paragenetic context, eleven polished thin sections from grey sandstones (GY-1~GY-9, DSC-08 and DSC-14; Table S2) were prepared for in situ sulfur isotope analyses, conducted with a Cameca 7f secondary ion mass spectrometer (SIMS) at the University of Manitoba, Winnipeg, Canada. Procedures similar to those documented by Hough et al. (2019) were used. All samples were gold coated to prevent surface charging. Sulfur isotope ratios ($^{34}S/^{32}S$) were measured, by using a ~1-nA Cs^+ primary beam accelerated at 10 kV with a spot size of ~15 μm filtered through a 247 μm entrance slit. The sulfur isotope values are reported in per mil relative to V-CDT standards with an analytical uncertainty (1σ) of ± 0.3‰ for $\delta^{34}S$.

Results

Uranium and thorium contents

Average U contents for red, green and yellow sandstones are 1.55 ppm, 1.32 ppm and 1.81 ppm, whereas the content for barren grey sandstones is 12.05 ppm (Tables S1 and S3). The oxidized and reduced sandstones have similar Th contents but differ in their Th/U ratios (Fig. S5). The mean ratio of Th/U in red, green and yellow sandstones are 7.68, 9.20 and 6.94, whereas the ratio in

This is the peer-reviewed, final accepted version for American Mineralogist, published by the Mineralogical Society of America.
The published version is subject to change. Cite as Authors (Year) Title. American Mineralogist, in press.
DOI: https://doi.org/10.2138/am-2021-7888. http://www.minsocam.org/

181 barren grey sandstones is 1.06 (Table S3).

182 **Redox-sensitive indicators of host sandstones**

183 In contrast to those in red and yellow sandstones, the Fe^{3+}/Fe^{2+} ratios are less than 1.0 in both
184 green and grey sandstones (Fig. 3a). The mean ratio of S_{total}/S^{2-} in red sandstones (mean > 6) is
185 much higher than that in yellow sandstones (mean = 1.80), and the mean value in grey sandstones
186 (mean = 1.40) is lower than that in green sandstones (mean = 3.74; Fig. 3a; Table S4). Both the
187 average values of S^{2-} and total organic carbon (TOC) are highest in mineralized grey sandstones,
188 followed by those in barren grey sandstones and yellow sandstones, and decreasing gradually from
189 those in green sandstones to those in red sandstones (Fig. 3b). Notably, there is a positive
190 correlation between TOC and S^{2-} in grey sandstones (Fig. 3b). There are relatively higher values
191 of ΔEh but lower pH in mineralized grey sandstones, and the pH values in all four colored
192 sandstone units are more than 7 (Fig. 3c).

193 **Occurrence and paragenesis of Fe-bearing minerals**

194 Macroscopically, the Fe-bearing minerals that can be found mainly include pyrite, limonite and
195 hematite (Fig. 4). Pyrite, generally as nodules with diameter ranging from 2 to 20 mm in drilling
196 cores, is predominantly associated with CD in the grey sandstone and surrounded by limonite when
197 exposed to air for an extended period of time (Fig. 4a). Limonite is a mixture of iron hydroxides,
198 mainly comprised of goethite, and usually occurs as encrustation on pyrite in the yellow sandstone
199 (Fig. 4d). The dark red hematite is mainly distributed in the red sandstone (Figs. 4b, 4c and 4e).

200 Microscopically, the Fe-bearing minerals appear mainly as authigenic and altered minerals such

as hematite, goethite, pyrite and chlorite, as well as detrital minerals such as Fe-Ti oxides and biotite (Fig. 5; Table S5). Hematite mainly occurs as dark red cements in the matrix or as coatings on mineral surfaces and along microfractures of clastic particles in red sandstones (Fig. 5a). Minor amounts of it occur as subhedral grains with a diameter up to 150 μm (Fig. 5b). Goethite can be observed in both yellow and red sandstones, and occurs primarily as coatings on the surfaces of interstitial materials and detrital particles, or along microfractures of clastic particles (Fig. 5c). Same as with hematite, a small amount of goethite was observed as subhedral grains (Fig. 5d).

Three different morphologies of pyrite in all four colored sandstones were identified: framboidal, euhedral and cement. Framboidal pyrite mainly distributed around CD is the most abundant type of pyrite (Fig. 5e). Densely-packed framboids appear as spherical aggregates of submicrometer-sized pyrite crystals. Euhedral pyrite, generally in the form of discrete cubes, is most closely associated with the matrix of clay minerals (Fig. 5f). Distributed between clastic particles, the pyrite cement shows a texturally homogeneous growth (Fig. 5g).

Chlorite is most abundant in the green sandstone, followed by the grey sandstone. It occurs mainly in one of two habits: pompon-like aggregates coating clastic particles (Fig. 5h), or needle-shaped crystals or squamous aggregates in the matrix (Fig. 5i).

The detrital Fe-Ti oxide minerals were observed in all four colored sandstone units (Fig. 5j). Ilmenite is the original detrital mineral but it usually appears as the remnant grain with residual cores surrounded by Ti oxides (Fig. 5k). These minerals are a mixture of Ti oxide and Fe oxide/hydroxide micrograins, characterized by relatively high U contents (Table S5). Iron-Ti

oxides are more abundant in grey sandstones than in oxidized sandstones in which the Fe-Ti oxides have lower iron contents (Table S5).

Detrital biotite is high in Fe but low in Mg (Table S5), and occurs in all four colored sandstone units (Fig. 5l). The length of the biotite can reach several hundred micrometers, and it generally appears as a deformed grain.

These six Fe-bearing minerals are closely related to each other, mainly manifested as the coexistence of two or more minerals at the micron scale (Fig. 6). Significantly, the types of Fe-bearing minerals occurring along cleavage planes in biotite in different colored sandstones are quite distinct. For instance, pyrite predominates in the grey sandstone (Fig. 6a), hematite in the red sandstone (Fig. 6b), and goethite in the yellow sandstone (Figs. 6c and 6d), whereas in the green sandstone, biotite was partially replaced by chlorite (Fig. 6e). In addition, it can also be observed that chlorite altered from biotite was filled with hematite and pyrite (Fig. 6f). As a clay mineral widely distributed in the matrix, chlorite occurrence is linked to the occurrence of pyrite (Fig. 6g). Generally, pyrite is distributed in the microfractures of or around Fe-Ti oxides (Figs. 6h and 6i). In red sandstones, framboidal hematite can be observed (Fig. 6j), whereas in yellow sandstones, goethite and pyrite are often found on the same particle (Figs. 6k and 6l), and the goethite around the edge of different morphological pyrite is documented (Fig. S6). In addition, based on our observations and recent work described in detail by Yue et al. (2020), it is common to see the framboidal pyrite overprinted by euhedral pyrite and pyrite cement, respectively, in mineralized grey sandstones (Fig. S7). The simplified paragenetic sequence of Fe-bearing minerals in the

This is the peer-reviewed, final accepted version for American Mineralogist, published by the Mineralogical Society of America.
The published version is subject to change. Cite as Authors (Year) Title. American Mineralogist, in press.
DOI: https://doi.org/10.2138/am-2021-7888. http://www.minsocam.org/

241 Dongsheng U deposit is illustrated in Figure 7.

242 **Proportions of pyrite**

243 The proportions of pyrite in reduced sandstones are 2 orders of magnitude higher than that in
244 oxidized sandstones. In red, green and yellow sandstone units, the mean area percentages of pyrite
245 are 1.49×10^{-4}%, 3.31×10^{-4}% and 5.47×10^{-4}%, respectively (Table S6). In mineralized grey
246 sandstones, the proportions of pyrite ranging from 3.97×10^{-2} to 9.28×10^{-2}% are higher than those
247 in barren grey sandstones (1.06×10^{-2} to 2.58×10^{-2}%) whose values represent the initial level of
248 pyrite content.

249 **In situ sulfur isotopes**

250 Sulfur isotopes were analyzed in pyrite from barren samples (pre-ore pyrite) and associated with
251 U (ore-stage pyrite; Fig. 8; Table S7). The pre-ore pyrite produced $\delta^{34}S$ values from -19.1 to +20.3‰
252 (mean = +7.3‰). Framboidal pyrite (n = 5) with ^{34}S depletion ranges from -19.1 to -8.0‰ (mean
253 = -13.4‰), whereas the euhedral and cement pyrite (n = 9), together with the pyrite occurring
254 along cleavage planes in biotite (n = 1) show higher values from +7.9 to +20.3‰ (mean = +17.7‰).
255 The $\delta^{34}S$ values of ore-stage pyrite (n = 29) range from -56.9 to -3.8‰ (mean = -34.1‰). Ore-
256 stage framboidal pyrite (n = 12) ranges from -31.2 to -3.8‰ (mean = -16.4‰), whereas ore-stage
257 euhedral and cement pyrite (n = 17) have lower values from -56.9 to -34.3‰ (mean = -46.7‰).

258 **Uranium mineralization**

259 Uranium minerals are closely related to pyrite and Fe-Ti oxides (Fig. 9), mainly distributed: (1)
260 in the interstices of microcrystallites of the closely arranged pyrite framboids (Figs. 9a-9c), (2)

This is the peer-reviewed, final accepted version for American Mineralogist, published by the Mineralogical Society of America.
The published version is subject to change. Cite as Authors (Year) Title. American Mineralogist, in press.
DOI: https://doi.org/10.2138/am-2021-7888. http://www.minsocam.org/

around the Fe-Ti oxides, euhedral pyrite or pyrite cement generally replacing the Fe-Ti oxides (Figs. 9d-9h), and (3) along cleavage planes in biotite filled with pyrite (Fig. 9i).

Discussion

Alteration of Fe-bearing minerals

The alteration among Fe-bearing minerals can be divided into: (1) alteration from Fe^{2+}-bearing to Fe^{2+}-bearing minerals, (2) oxidation from Fe^{2+}-bearing to Fe^{3+}-bearing minerals, and (3) reduction from Fe^{3+}-bearing to Fe^{2+}-bearing minerals. The multiple alteration processes not only represent the changes of redox environment, but also indicate the multi-stage mobilization and fixation of U (e.g., Reynolds and Goldhaber 1978; Reynolds et al. 1986; Bonnetti et al. 2015; Jiao et al. 2018b; Zhang et al. 2019a).

The alteration from Fe^{2+}-bearing to Fe^{2+}-bearing minerals generally involves: (1) biotite chloritization, and (2) the formation of pyrite whose Fe sources may be biotite, chlorite, Fe-Ti oxides and dissolved Fe^{2+} carried by the descending meteoric water. The alteration of biotite is closely related to the physico-chemical properties of pore fluids (Boles and Johnson 1983; Claeys and Mount 1991). Biotite can be replaced pseudomorphically by chlorite with a greenish tint (Fig. 6e), which may indicate the conditions of low K^+/H^+ ratios relative to $(Fe^{2+} + Mg^{2+})/H^+$ ratios (Veblen and Ferry 1983; Morad 1986; Morad and Aldahan 1986).

The euhedral pyrite was formed along cleavage planes in biotite, thus indicating high rates of iron leaching and low rates of Fe^{2+} supply during the dissolution of biotite (Morad 1986; Fig. 6a; Table S5: Biotite, GY-11). Additionally, the lower iron content in chlorite (Table S5: Chlorite, GY-

This is the peer-reviewed, final accepted version for American Mineralogist, published by the Mineralogical Society of America.
The published version is subject to change. Cite as Authors (Year) Title. American Mineralogist, in press.
DOI: https://doi.org/10.2138/am-2021-7888. http://www.minsocam.org/

281 5) associated with pyrite permits the interpretation that the released iron was utilized in the
282 formation of pyrite (Fig. 6g). Previous studies have demonstrated that the substitution of Mg^{2+} for
283 Fe^{2+} after the precipitation of chlorite results in a low Fe/(Fe + Mg) ratio in chlorite under
284 conditions of high Mg^{2+} activities. Pyrite is formed in an anoxic-sulfidic environment due to the
285 released Fe^{2+} (White et al. 1985; Aldahan and Morad 1986). Thermodynamic calculations
286 performed by Bonnetti et al. (2015) suggested that ilmenite is almost insoluble in the H_2S-free
287 system over a broad range of pH conditions (approximately from 5 to 11), whereas Fe-Ti oxide
288 grains (predominantly ilmenite) will be altered to Ti-oxide minerals and release Fe^{2+} in the
289 presence of H_2S-rich fluids during diagenesis, which is involved in the following reaction
290 (Reynolds and Goldhaber 1978; Bonnetti et al. 2015):

291 $$FeTiO_3 + 2H_2S \rightarrow TiO_2 + FeS_2 + H_2O + H_2 \quad (1)$$

292 The alteration of ilmenite is usually accompanied by the production of relatively large micropores
293 generally filled with pyrite (Fig. 6h). Additionally, due to Fe-Ti oxides containing minor U (Table
294 S5), the U will also be leached out during alteration, and precipitate as U-bearing minerals around
295 the Fe-Ti oxides (Figs. 9g and 9h).

296 Epigenetic U mineralization is generally considered as a continuous process driven by the
297 translation of the redox front (Bonnetti et al. 2020). There will definitely be a part of dissolved
298 Fe^{2+} not incorporated into Fe^{3+}-bearing minerals, thereby providing iron source for ore-stage pyrite.
299 The whole process is supported by the mineralized grey sandstones having the highest pyrite
300 contents and the red sandstones with the lowest (Table S6). In addition, the dissolved U from

This is the peer-reviewed, final accepted version for American Mineralogist, published by the Mineralogical Society of America.
The published version is subject to change. Cite as Authors (Year) Title. American Mineralogist, in press.
DOI: https://doi.org/10.2138/am-2021-7888. http://www.minsocam.org/

oxidized sandstones will precipitate as coffinite and uraninite around the pyrite in grey sandstones (Fig. 9). This process will be further discussed in the next section.

The alteration from Fe^{2+}-bearing to Fe^{3+}-bearing minerals usually results in the precipitation of goethite and/or hematite from pyrite oxidation mainly involving chemical, biological and electrochemical reactions (Lowson 1982; Evangelou and Zhang 1995). Because the activity of ferro-oxidizing bacteria is greatly reduced with a pH of over 4.5 (Kuznetsov et al. 1963; Rackley 1972), pyrite oxidation is dominated by abiotic chemical reactions in sandstones of the lower member of the Zhiluo Formation (Fig. 3c: pH >7). The process can be illustrated by following reactions (Evangelou and Zhang 1995):

$$FeS_2 + 7/2O_2 + H_2O \rightarrow Fe^{2+} + 2SO_4^{2-} + 2H^+ \quad (2)$$

$$Fe^{2+} + 1/4O_2 + H^+ \rightarrow Fe^{3+} + 1/2H_2O \quad (3)$$

$$Fe^{3+} + 3H_2O \rightarrow Fe(OH)_{3(s)} + 3H^+ \quad (4)$$

$$FeS_2 + 7Fe_2(SO_4)_3 + 8H_2O \rightarrow 15FeSO_4 + 8H_2SO_4 \quad (5)$$

$$Fe(OH)_{3(s)} \rightarrow FeOOH + H_2O \quad (6)$$

$$2FeOOH \rightarrow Fe_2O_3 + H_2O \quad (7)$$

Factors such as pH, O_2 content, morphology and specific surface of pyrite, as well as hydrological conditions, determine the rate of oxidation (Moses et al. 1987; Nicholson et al. 1990; Evangelou and Zhang 1995), and the final product is dependent on the magnitude of the rate of oxidation. Goethite is the early product (in the reaction 6; Figs. 6k and 6l), and the build-up of goethite around the edge of a particle will decrease rate of pyrite oxidation because of the limitation of oxygen

321 diffusion through the armoring effect (Nicholson et al. 1990; Heidari et al. 2017; Mahoney et al.
322 2019). However, it is the metastable step under arid climate conditions, and goethite can be
323 transformed to hematite by dehydration reaction (in the reaction 7; Fig. 6j; e.g., Walker 1967), thus
324 giving the sandstone reddish color. Therefore, the large-scale distribution of hematite in the altered
325 sandstone with shallow burial (< 800 m) indicates the semi-arid to arid climate, which may also
326 facilitate the dissolution of U (Hobday and Galloway 1999; Bonnetti et al. 2020). Uranium trapped
327 by Fe-Ti oxides, CD and clay minerals together with the primary U originating from intermediate-
328 acid magmatic rocks (U-rich granites; e.g., Zhang et al. 2016) of the Yinshan orogenic belt lying
329 to the north of the basin provide significant sources for the U mineralization in the Dongsheng
330 deposit (Jiao et al. 2006, 2015), as the regional U geochemical background in barren grey
331 sandstones (U_{mean} = 12.05 ppm) is much higher than the average in the upper continental crust
332 (U_{mean} = 2.8 ppm; Cuney 2010). Additionally, in outcrops, the pyrite in reduced sandstones was
333 oxidized to goethite, leading to a wide distribution of yellow sandstones due to the relatively weak
334 oxidizing capability of modern weathering (lower S_{total}/S^{2-} ratio but higher U, TOC and pyrite
335 contents in yellow sandstones than those in red sandstones; Fig. 3; Tables S3 and S6). Meanwhile,
336 the U-bearing minerals in mineralized grey sandstones were oxidized, and the dissolved U flowed
337 down the sandstones with the groundwater, and was re-adsorbed on organic materials (e.g., the CD
338 in the Zhiluo Formation or the coal seams in the Yan'an Formation) nearby (Figs. 1c-1e; Zhang et
339 al. 2019a).

340 The reduction (Fe^{3+}-bearing to Fe^{2+}-bearing minerals) mainly involves the formation of

authigenic chlorite from hematite. According to pollen analyses, the Hetao graben along the north margin of the basin was formed at least since Late Paleocene (Fu et al. 1994), thus cutting off the sources of U and leading to the termination of large-scale U mineralization (Zheng et al. 2006; Miao et al. 2010; Li et al. 2016). Subsequently, the decrease of oxygenated groundwater led to large amounts of ascending hydrocarbons from the Paleozoic and the early Mesozoic strata, which created a reducing environment (Zhao et al. 1996). Infiltration of hydrocarbons in red sandstones resulted in the reduction of hematite into chlorite (e.g., Zhang et al. 2019), which was evidenced by red calcareous nodules within green sandstones (Figs. 1b-1d and 2b), the similar contents of U and pyrite between red and green sandstones (Tables S3 and S6), and the hematite surrounded by chlorite (Fig. 6f).

Genesis of the Dongsheng uranium deposit

Different from the well-established model of roll front-type U deposits (Granger and Warren 1969; Warren 1971, 1972; Reynolds and Goldhaber 1983; Cuney 2009; Bonnetti et al. 2015; Hough et al. 2019), tabular orebodies occur at a regional density-stabilized oxidation-reduction interface (Northrop et al. 1990; Sanford 1990, 1992, 1994; Hansley and Spirakis 1992; Turner et al. 1993; Abzalov 2012). In this occurrence, oxidizing fluids were derived from oxygenated U-bearing meteoric water, whereas reducing fluids were closely associated with organic matter composed of inherent organic materials (such as plant fragments in the Cottonwood Wash U-V tabular deposits, USA; Meunier et al. 1987) in sandstones, and extrinsic humic acid-bearing pore waters (the Grants U region, USA; Turner et al. 1993) from adjacent strata. In the Dongsheng

deposit, due to abundant hydrocarbons in the oil-, gas- or coal-bearing strata underlying the Zhiluo Formation and the inherent CD in the grey sandstone (Jiao et al. 2015; Zhang et al. 2019a), the numerical modeling of fluid flow reported by Xue et al. (2010) indicated that the mixing of descending meteoric fluids and ascending hydrocarbons are responsible for U mineralization. Additionally, the combination of a stable tectonic period followed by regional uplift and an alternating climate from humid to arid is most favorable for ore deposition (Harshman and Adams 1980; Jiao et al. 2015; Bonnetti et al. 2020).

Based on the development of the Ordos Basin and its sedimentary sequences, the sulfur involved in the formation of ore-stage pyrite in the Zhiluo Formation hosting the Dongsheng deposit may be derived from: (1) dissolved sulfate ions from Ordovician marine evaporites, (2) H_2S/HS^- in extrinsic hydrocarbons, or (3) oxidation of pre-ore pyrite, whose sulfur mainly results from the weathering of volcanic and metamorphic rocks in source area (e.g., Jiao et al. 2015). Because the sandstones of the Zhiluo Formation overlie the Ordovician evaporites by > 2000 m (Li et al. 1984; Yang et al. 2004), there is a sufficient distance for the upward-migrating fluids containing dissolved SO_4^{2-} could be completely consumed by microbial reduction or purely chemical processes in the oil- and coal-bearing late Paleozoic to early Mesozoic sediments. Jiao et al. (2018b) has reported that in outcrops, the majority of pyrite occurs within approximately 4 m of the top of coal seams of the Yan'an Formation, and the farther away from the coal seam, the smaller size of and the less numerous of pyrite grains become in sandstones. This suggests that the formation and distribution of this pyrite is intimately related to H_2S escaped from coal seams (Jiao et al. 2018b), and the H_2S

This is the peer-reviewed, final accepted version for American Mineralogist, published by the Mineralogical Society of America.
The published version is subject to change. Cite as Authors (Year) Title. American Mineralogist, in press.
DOI: https://doi.org/10.2138/am-2021-7888. http://www.minsocam.org/

seems to be completely fixed within 4 m. However, the orebodies are generally more than 20 m away from the boundary between the Zhiluo and the Yan'an Formation (Fig. 2; Peng et al. 2019). Therefore, it is impossible to have enough H_2S/HS^- in extrinsic hydrocarbons to produce ore-stage pyrite, which can also be supported by very little pyrite in green sandstones (Table S6). Therefore, the oxidation of pre-ore pyrite becomes a dominant sulfur source for ore-stage pyrite.

Despite the hydrothermal conditions inferred from fluid inclusions in calcite cements (Xiao et al. 2004; Cao et al. 2016; Akhtar et al. 2017), vitrinite reflectance (R_o < 0.47%) of CD in mineralized grey sandstones suggests mineralization took place at temperatures below 65 ℃ (Zhang et al. 2019b). The lower $\delta^{34}S$ of ore-stage euhedral and cement pyrite ($\delta^{34}S$ = -56.9 to -34.3‰) than those of ore-stage framboidal pyrite ($\delta^{34}S$ = -31.2 to -3.8‰), together with their paragenetic relationship (Fig. S7) indicate that the different pyrite textural generations may form through distinct mechanisms, rather than a biogeochemical cycle (e.g., Bonnetti et al. 2020). We propose that ore-stage framboids were produced through bacterial sulfate reduction (BSR), and the following formation of ore-stage euhedral and cement pyrite was via abiogenic Ostwald ripening (Fig. 10).

Sulfate ions (SO_4^{2-}) derived from pyrite oxidation were reduced to H_2S/HS^- by BSR and formed ore-stage framboidal pyrite (Fig. 10; Machel 2001), which is also supported by the positive correlation between S^{2-} and TOC in grey sandstones (Reynolds et al. 1982; Fig. 3b). In this process, the bacteria confirmed to be in existence in the Dongsheng deposit prefer the lighter ^{32}S isotope (Bruchert 2004; Seal 2006; Jiang et al. 2012; Gregory and Kohn 2020), thus meaning that the

401 biogenic pyrite will have a lower $\delta^{34}S$ value than subsequent generations. In a closed system for
402 sulfur, the Rayleigh fractionation may be exhibited, leading to a fraction of framboidal pyrite
403 produced $\delta^{34}S$ values higher than pre-ore pyrite (Fig. 8), as predicted by Hough et al. (2019).
404 Additionally, hydrogen ions produced by organic matter degradation during BSR can be removed
405 by destruction of feldspars and carbonate (e.g., Bonnetti et al. 2015), which has contributed to the
406 maintained pH at relatively high values (Fig. 3c). The dissolution of feldspars explains the
407 abundance of kaolinite in the mineralized zone and will supply a silica source for the formation of
408 coffinite (Langmuir 1978).

409 There are also sulfite and thiosulfate ions generated by pyrite oxidation in neutral to basic
410 solutions (Granger and Warren 1969), and the unstable sulfur species will spontaneously undergo
411 decomposition by disproportionation resulting in ^{34}S-depleted HS^- and ^{34}S-enriched sulfate (Fig.
412 S8; Granger and Warren 1969; Hough et al. 2019). Pyrite framboid is the metastable phase, and
413 existing surfaces of pyrite have been identified to be conducive to precipitation of pyrite of later
414 stages (Sawlowicz 1993). The ^{34}S-depleted HS^- produced from dissolved framboidal crystals was
415 utilized to generate euhedral and cement pyrite (Fig. 10). This process could be revealed through
416 observations in which framboidal pyrite was being transformed to euhedral or cement pyrite via
417 Ostwald ripening (Fig. S7; e.g., Morse and Casey 1988; Steefel and Cappellen 1990). Because the
418 ^{34}S-enriched sulfate is nonreactive in abiogenic process and removed by groundwater, the pyrite
419 formed through Ostwald ripening will always have lower $\delta^{34}S$ values than pre-existing or earlier-
420 formed pyrite (Fig. 10; Brunner and Bernasconi 2005), which is evidenced by the very low isotopic

421 values of euhedral and cement pyrite ranging from -56.9 to -34.3‰, lower than any values of
422 framboidal pyrite. The sulfur isotopes of abiogenically-derived pyrite are dependent on Eh/pH
423 conditions established by the presence of barite and clausthalite coupled with alternating
424 precipitation between pyrite and ferroselite (Figs. S9 and S10; Ohmoto 1972). The process of
425 producing euhedral grains of pyrite with very low $\delta^{34}S$ values via Ostwald ripening in the
426 Dongsheng deposit is on contrast to sulfur recycling processes suggested by Hough et al. (2019)
427 for the Wyoming roll front U deposits.

428 **Implications**

429 In sandstone-type U deposits, the mobilization, migration and fixation of U are driven by
430 multiple redox events in low-temperature conditions, which can be directly and effectively
431 documented in textures, paragenetic sequence and chemical compositions of various Fe-bearing
432 minerals. Several alteration processes among Fe-bearing minerals not only give sandstones distinct
433 colors (e.g., red, green and yellow), considered as a criterion for ore prospecting, but provide a
434 minor U source for mineralization (e.g., Fe-Ti oxides, Bonnetti et al. 2015), and can be used to
435 effectively assess the sulfur source of pyrite closely associated with U-bearing minerals.
436 Additionally, textural and sulfur isotopic data provide new insights into the genetic mechanism of
437 ore-stage pyrite in the Dongsheng deposit. Both biogenic and abiogenic mechanisms were
438 involved in the generation of ore-stage pyrite. Namely, framboidal pyrite was produced by BSR,
439 using the sulfur derived from oxidation of pre-ore pyrite, whereas Ostwald ripening was
440 responsible for the formation of euhedral and cement pyrite from framboids. Although the redox

441 mechanism of the Dongsheng deposit is slightly different from that of deposits in Lake Eyre Basin,
442 Australia (BSR overprinted by hydrothermal fluids, Ingham et al. 2014), deposits in Wyoming,
443 USA (pyrite recycling, Hough et al. 2019) and deposit in Erlian Basin, China (biogenic processes,
444 Bonnetti et al. 2020), which may result from different geologic contexts, the role of bacterial
445 metabolic processes was proposed for all these sandstone-type U deposits, and a biogenic
446 mechanism was considered to be the common and/or initial stage of U mineralization. The
447 alteration processes related to Fe and U of the Dongsheng deposit during the mineralization period
448 are also similar to those of other sandstone-type U deposits (e.g., Warren 1971; Rong et al. 2016),
449 except for the superimposed effects of post-ore hydrocarbon-rich fluids (Miao et al. 2010; Peng et
450 al. 2019) and surface weathering (Jiao et al. 2018b). This study also demonstrates that the careful
451 assessment of U in the context of other redox sensitive elements like Fe and S can provide a more
452 complete picture of the formation of U ore deposits, and the transformation model of Fe-bearing
453 minerals proposed for the Dongsheng deposit may be applied to other mineral resources controlled
454 by redox events.

455 **Acknowledgements**

456 We are grateful to Zhenpeng Tao, Aisheng Miao, Xiaoquan Jiao and other workers from the
457 Geological Party No.208, CNNC for help with fieldwork, and we also thank Longyao Xiong, Zefu
458 Yan and Qiang Li for suggestion to figure editing, Ryan Sharpe for assisting with the SIMS analysis,
459 and Yonggang Gao for language polishing. Finally, the authors would like to thank Paul Tomascak
460 and two anonymous reviewers for constructive and insightful suggestions that greatly improved

461 this manuscript.

462 **Funding**

463 Financial support for this study was provided by the National Key Research and Development
464 Program of China (No. 2018YFC0604202), the State Scholarship Fund from the China
465 Scholarship Council (No. 201906410063) and a NSERC Discovery grant to Fayek.

466 **References cited**

467 Abzalov, M.Z. (2012) Sandstone-hosted uranium deposits amenable for exploitation by in situ
468 leaching technologies. Applied Earth Science, 121, 55-64.

469 Akhtar, S., Yang, X.Y., and Pirajno, F. (2017) Sandstone type uranium deposits in the Ordos Basin,
470 Northwest China: A case study and an overview. Journal of Asian Earth Sciences, 146, 367-
471 382.

472 Aldahan, A.A., and Morad, S. (1986) Chemistry of detrital biotites and their phyllosilicate
473 intergrowths in sandstones. Clay and Clay Minerals, 34, 539-548.

474 Boles, J.R., and Johnson, S.K. (1983) Influence of mica surfaces on pore water pH. Chemical
475 Geology, 43, 303-317.

476 Bonnetti, C., Cuney, M., Michels, R., Truche, L., Malartre, F., Liu, X.D., and Yang, J.X. (2015)
477 The multiple roles of sulfate-reducing bacteria and Fe-Ti oxides in the genesis of the
478 Bayinwula roll front-type uranium deposit, Erlian Basin, NE China. Economic Geology, 110,
479 1059-1081.

480 Bonnetti, C., Zhou, L.L., Riegler, T., Brugger, J., and Fairclough, M. (2020) Large S isotope and

481 trace element fractionations in pyrite of uranium roll front systems result from internally-
482 driven biogeochemical cycle. Geochimica et Cosmochimica Acta, 282, 113-132.
483 Bruchert, V. (2004) Physiological and ecological aspects of sulfur isotope fractionation during
484 bacterial sulfate reduction. Geological Society of America, Special Paper 379, p. 1-16.
485 Brunner, B., and Bernasconi, S.M. (2005) A revised isotope fractionation model for dissimilatory
486 sulfate reduction in sulfate reducing bacteria. Geochimica et Cosmochimica Acta, 69, 4759-
487 4771.
488 Cai, C.F., Dong, H.L., Li, H.T., Xiao, X.J., Qu, G.X., and Zhang, C.M. (2007a) Mineralogical and
489 geochemical evidence for coupled bacterial uranium mineralization and hydrocarbon
490 oxidation in the Shashagetai deposit, NW China. Chemical Geology, 236, 167-179.
491 Cai, C.F., Li, H.T., Qin, M.K., Luo, X.R., Wang, F.Y., and Ou, G.X. (2007b) Biogenic and
492 petroleum-related ore-forming processes in Dongsheng uranium deposit, NW China. Ore
493 Geology Reviews, 32, 262-274.
494 Cao, B.F., Bai, G.P., Zhang, K.X., Zhang, L.K., and He, B. (2016) A comprehensive review of
495 hydrocarbons and genetic model of the sandstone-hosted Dongsheng uranium deposit, Ordos
496 Basin, China. Geofluids, 16, 624-650.
497 Chen, G., Li, X.P., Zhou, L.F., Li, S.H., Li, X.D., and Zhang, H.R. (2005) Ordos basin tectonics
498 relative to the coupling coexistence of multiple energy resources. Earth Science Frontiers, 12,
499 535-541 (in Chinese with English abstract).
500 Chen, Z.Y. (2002) Regional distribution regularity of sandstone uranium deposits in Asian

continent and prospecting strategy for sandstone uranium deposits in China. Uranium Geology, 18, 129-137 (in Chinese with English abstract).

Claeys, P.F., and Mount, J.F. (1991) Diagenetic origin of carbonate, sulfide and oxide inclusions in biotites of the Great Valley Group (Cretaceous), Sacramento Valley, California. Journal of Sedimentary Research, 61, 719-731.

Cuney, M. (2009) The extreme diversity of uranium deposits. Mineralium Deposita, 44, 3-9.

Cuney, M. (2010) Evolution of uranium fractionation processes through time: Driving the secular variation of uranium deposit types. Economic Geology, 105, 553-569.

Deng, J., Wang, Q.F., Gao, B.F., Huang, D.H., Yang, L.Q., Xu, H., and Zhou, Y.H. (2005) Evolution of the Ordos Basin and its distribution of various energy and mineral resources. Geoscience, 19, 538-545 (in Chinese with English abstract).

Douglas, G.B., Butt, C.R.M., and Gray, D.J. (2011) Geology, geochemistry and mineralogy of the lignite-hosted Ambassador palaeochannel uranium and multi-element deposit, Gunbarrel Basin, Western Australia. Mineralium Deposita, 46, 761-787.

Evangelou, V.P., and Zhang, Y.L. (1995) A review: Pyrite oxidation mechanisms and acid mine drainage prevention. Critical Reviews in Environmental Science and Technology, 25, 141-199.

Fu, Z.Y., Yuan, X.Q., and Geng, G.C. (1994) The tertiary of the Hetao Basin and its biotas. Journal of Stratigraphy, 18, 24-29.

Goldhaber, M.B., Reynolds, R.L., and Rye, R.O. (1983) Role of fluid mixing and fault-related

sulfide in the origin of the Ray Point uranium district, south Texas. Economic Geology, 78, 1043-1063.

Granger, H.C., and Warren, C.G. (1969) Unstable sulfur compounds and the origin of roll-type uranium deposits. Economic Geology, 64, 160-171.

Gregory, D.D., and Kohn, M.J. (2020) Pyrite: Fool's gold records starvation of bacteria. American Mineralogist, 105, 282-283.

Guo, X.J., and Jiao, G.H. (2002) Petroleum Geology of Paleozoic in the North China: Beijing, Geological Publishing House, 171 p (in Chinese).

Han, X.Z., Zhang, Z.L., Yao, C.L., Li, X.D., Li, S.X., Miao, A.S., and Yang, J.X. (2008) Discussion on metallogenic model for sandstone-hosted uranium deposits in northeastern Ordos Basin. Mineral Deposits, 27, 415-422 (in Chinese with English abstract).

Hansley, P.L., and Spirakis, C.S. (1992) Organic matter diagenesis as the key to a unifying theory for the genesis of tabular uranium-vanadium deposits in the Morrison Formation, Colorado Plateau. Economic Geology, 87, 352-365.

Harshman, E.N., and Adams, S.S. (1980) Geology and recognition criteria for roll-type uranium deposits in continental sandstones. U.S. Department of Energy GJBX-1 81, 185 p.

He, Z.X. (2003) Evolution of Ordos basin with relation to oil and gas: Beijing, Petroleum Industry Press, p. 3-143 (in Chinese).

Heidari, P., Li, L., Jin, L.X., Williams, J.Z., and Brantley, S.L. (2017) A reactive transport model for Marcellus shale weathering. Geochimica et Cosmochimica Acta, 217, 421-440.

541 Hobday, D.K., and Galloway, W.E. (1999) Groundwater processes and sedimentary uranium
542 deposits. Hydrogeology Journal, 7, 127-138.
543 Hough, G., Swapp, S., Frost, C., and Fayek, M. (2019) Sulfur isotopes in biogenically and
544 abiogenically derived uranium roll-front deposits. Economic Geology, 114, 353-373.
545 Huang, J.B., and Huang, S.J. (2005) Regional metallogenic characteristics of China's uranium
546 resources. Uranium Geology, 21, 129-138 (in Chinese with English abstract).
547 Ingham, E.S., Cook, N.J., Cliff, J., Ciobanu, C.L., and Huddleston, A. (2014) A combined chemical,
548 isotopic and microstructural study of pyrite from roll-front uranium deposits, Lake Eyre Basin,
549 South Australia. Geochimica et Cosmochimica Acta, 125, 440-465.
550 Jia, J.D., He, G.Q., Li, M.S., Zhou, D.C., and Zhang, L.X. (1997) Structural feature of basement
551 in the Ordos Basin and its control to Paleozoic gas. Geological Journal of China Universities,
552 3, 144-153 (in Chinese with English abstract).
553 Jiang, L., Cai, C.F., Zhang, Y.D., Mao, S.Y., Sun, Y.G., Li, K.K., Xiang, L., and Zhang, C.M. (2012)
554 Lipids of sulfate-reducing bacteria and sulfur-oxidizing bacteria found in the Dongsheng
555 uranium deposit. Chinese Science Bulletin, 57, 1311-1319 (in Chinese with English abstract).
556 Jiao, Y.Q., Chen, A.P., Wang, M.F., Wu, L.Q., Yuan, H.T., Yang, Q., Zhang, C.Z., and Xu, Z.C.
557 (2005a) Genesis analysis of the bottom sandstone of Zhiluo Formation, northeastern Ordos
558 Basin: Predictive base of spatial orientation of sandstone-type uranium deposit. Acta
559 Sedimentologica Sinica, 23, 371-379 (in Chinese with English abstract).
560 Jiao, Y.Q., Wu, L.Q., Wang, M.F., and Xu, Z.C. (2005b) Forecasting the occurrence of sandstone-

561 type uranium deposits by spatial analysis: an example from the northeastern Ordos Basin,
562 China. In: Mao JW, Bierlein FP (eds) Mineral Deposit Research: Meeting the Global
563 Challenge. Springer-Verlag, Berlin Heidelberg, p. 273-275.
564 Jiao, Y.Q., Wu, L.Q., Yang, S.K., Lü, X.B., Yang, Q., Wang, Z.H., and Wang, M.F. (2006)
565 Sedimentology of uranium reservoir: The foundation of sandstone type uranium deposit
566 exploration and development: Beijing, Geological Publishing House, p. 265-267 (in Chinese).
567 Jiao, Y.Q., Wu, L.Q., Peng, Y.B., Rong, H., Ji, D.M., Miao, A.S., and Li, H.L. (2015) Sedimentary-
568 tectonic setting of the deposition-type uranium deposits forming in the Paleo-Asian tectonic
569 domain, North China. Earth Science Frontiers, 22, 189-205 (in Chinese with English abstract).
570 Jiao, Y.Q., Wu, L.Q., and Rong, H. (2018a) Model of inner and outer reductive media within
571 uranium reservoir sandstone of sandstone-type uranium deposits and its ore-controlling
572 mechanism: Case studies in Daying and Qianjiadian uranium deposits. Earth Science, 43,
573 459-474 (in Chinese with English abstract).
574 Jiao, Y.Q., Wu, L.Q., Rong, H., Zhang, F., Yue, L., Tao, Z.P., and Sun, Y.H. (2018b) Geological
575 modeling of uranium reservoir: the geological foundation of revealing the metallogenic
576 mechanism and solving “remaining uranium”. Earth Science, 43, 3568-3583 (in Chinese with
577 English abstract).
578 Kuznetsov, S.I., Ivanov, M.V., and Lyalikova, N.N. (1963) Introduction to geological microbiology:
579 International series in the earth sciences [translated from Vvedeniye v Geologicheskuyu
580 Mikrobiologiyu, Academy of Sciences: Moscow, USSR Press, 1962]: New York, McGraw-

Hill, 252 p.

Langmuir, D. (1978) Uranium solution-mineral equilibria at low temperatures with applications to sedimentary ore deposits. Geochimica et Cosmochimica Acta, 42, 547-569.

Li, S., Yang, S., and Jerzykiewicz, T. (1995) Upper Triassic-Jurassic foreland sequences of the Ordos basin in China. In: Dorobek SL, Ross GM (eds) Stratigraphic evolution of foreland basins: SEPM Special Publication 52, p. 233-241.

Li, S.T., Yang, S.G., and Lin, C.S. (1992) On the chronostratigraphic framwork and basic building blocks of sedimentary basin. Acta Sedimentologica Sinica, 10, 11-22 (in Chinese with English abstract).

Li, X.D., Yi, C., Gao, H.W., Chen, X.L., Zhang, K., and Wang, M.T. (2016) Study on formation mechanism of epigenetic altered zone in Zhiluo Formation, northeastern Ordos Basin, north China. Geoscience, 30, 739-747 (in Chinese with English abstract).

Li, Y.T., Sun, X.Y., and Liu, J.Y. (1984) Stratigraphy of China – the tertiary system of China. Beijing, Geological Publishing House, p. 116–119 (in Chinese).

Liu, C.Y., Zhao, H.G., and Sun, Y.Z. (2009) Tectonic background of Ordos Basin and its controlling role for basin evolution and energy mineral deposits. Energy Exploration & Exploitation, 27, 15-27.

Liu, S., and Yang, S. (2000) Upper Triassic-Jurassic sequence stratigraphy and its structural controls in the western Ordos Basin, China. Basin Research, 12, 1-18.

Lowson, R.T. (1982) Aqueous oxidation of pyrite by molecular oxygen. Chemical Reviews, 82,

461-497.

Machel, H.G. (2001) Bacterial and thermochemical sulfate reduction in diagenetic settings-old and new insights. Sedimentary Geology, 140, 143-175.

Mahoney, C., Marz, C., Buckman, J., Wagner, T., and Velandia, V.O.B. (2019) Pyrite oxidation in shales: Implications for palaeo-redox proxies based on geochemical and SEM-EDX evidence. Sedimentary Geology, 389, 186-199.

Meunier, J.D., Landais, P., Monthioux, M., and Pagel, M. (1987) Oxidation-reduction processes in the genesis of the uranium-vanadium tabular deposits of the Cottonwood Wash mining area (Utah, USA): evidence from petrological study and organic matter analysis. Bulletin de Minéralogie, 110, 145-156.

Miao, A.S., Jiao, Y.Q., Chang, B.C., Wu, L.Q., Rong, H., and Liu, Z.B. (2010) Detailed investigation of the paleo-interlayer-oxidation zone of Dongsheng uranium deposit in northeastern Ordos Basin. Geological Science and Technology Information, 29, 55-61 (in Chinese with English abstract).

Morad, S. (1986) Pyrite-chlorite and pyrite-biotite relations in sandstones. Sedimentary Geology, 49, 177-192.

Morad, S., and Aldahan, A.A. (1986) Diagenetic alteration of detrital biotite in Proterozoic sedimentary rocks from Sweden. Sedimentary Geology, 47, 95-107.

Morse, J.W., and Casey, W.H. (1988) Ostwald processes and mineral paragenesis in sediments. American Journal of Science, 288, 537-560.

621 Moses, C.O., Nordstrom, D.K., Herman, J.S., and Mills, A.L. (1987) Aqueous pyrite oxidation by
622 dissolved oxygen and by ferric iron. Geochimica et Cosmochimica Acta, 51, 1561-1671.
623 Nicholson, R.V., Gillham, R.W., and Reardon, E.J. (1990) Pyrite oxidation in carbonate-buffered
624 solution: 2. Rate control by oxide coatings. Geochimica et Cosmochimica Acta, 54, 395-402.
625 Northrop, H.R., Goldhaber, M.B., Landis, G.P., and Unruh, J.W. (1990) Genesis of the tabular-
626 type vanadium-uranium deposits of the Henry Basin, Utah; Part I, Geochemical and
627 mineralogical evidence for the sources of ore-forming fluids. Economic Geology, 85, 215-
628 236.
629 OECD-NEA, IAEA. (2010) Uranium 2009: resources, production and demand.
630 Ohmoto, H. (1972) Systematics of sulfur and carbon isotopes in hydrothermal ore deposits.
631 Economic Geology, 67, 551-578.
632 Peng, Y.B., Jiao, Y.Q., and Chen, A.P. (2019) Theoretical & technological innovation of uranium
633 mineralization and major prospecting breakthrough of Mesozoic uranium-bearing basins in
634 midwestern Inner Mongolia: Wuhan, China University of Geosciences Press, p. 14-30 (in
635 Chinese).
636 Qu, H.J., Li, W.H., Mei, Z.C., and Chen, Q.H. (2003) Relationship between sequence stratigraphy
637 and petroleum system in oil and gas exploration: An example in the Mesozoic Ordos Basin.
638 Geological Review, 49, 495-500 (in Chinese with English abstract).
639 Rackley, R.I. (1972) Environment of Wyoming Tertiary uranium deposits. American Association
640 of Petroleum Geologists Bulletin, 56, 755-774.

Reynolds, R.L., Fishman, N.S., Scott, J.H., and Hudson, M.R. (1986) Iron-titanium oxide minerals and magnetic susceptibility anomalies in the Mariano Lake-Lake Valley cores—Constraints on conditions of uranium mineralization in the Morrison Formation, San Juan Basin, New Mexico. In: Turner-Peterson CE, Santos ES, Fishman NS (eds) A Basin Analysis Case Study: The Morrison Formation Grants Uranium Region New Mexico. AAPG Bulletin, 22, 303-313.

Reynolds, R.L., and Goldhaber, M.B. (1978) Origin of a south Texas roll-type uranium deposit: I. Alteration of iron-titanium oxide minerals. Economic Geology, 73, 1677-1689.

Reynolds, R.L., and Goldhaber, M.B. (1983) Iron disulfide minerals and the genesis of roll-type uranium deposits. Economic Geology, 78, 105-120.

Reynolds, R.L., Goldhaber, M.B., and Carpenter, D.J. (1982) Biogenic and nonbiogenic ore-forming processes in the south Texas uranium district: Evidence from the Panna Maria deposit. Economic Geology, 77, 541-556.

Rong, H., Jiao, Y.Q., Wu, L.Q., Ji, D.M., Li, H.L., Zhu, Q., Cao, M.Q., Wang, X.M., Li, Q.C., and Xie, H.L. (2016) Epigenetic alteration and its constraints on uranium mineralization from the Qianjiadian uranium deposit, southern Songliao Basin. Earth Science, 41, 153-166 (in Chinese with English abstract).

Sanford, R.F. (1990) Hydrogeology of an ancient arid closed basin: Implications for tabular sandstone-hosted uranium deposits. Geology, 18, 1099-1102.

Sanford, R.F. (1992) A new model for tabular-type uranium deposits. Economic Geology, 87, 2041-2055.

661 Sanford, R.F. (1994) A quantitative model of ground-water flow during formation of tabular
662 sandstone uranium deposits. Economic Geology, 89, 341-360.
663 Sawlowicz, Z. (1993) Pyrite framboids and their development: a new conceptual mechanism.
664 Geologische Rundschau, 82, 148-156.
665 Seal, R.R. (2006) Sulfur isotope geochemistry of sulfide minerals. Reviews in Mineralogy and
666 Geochemistry, 61, 633-677.
667 Shawe, D.R., and Granger, H.C. (1965) Uranium ore rolls—An analysis. Economic Geology, 60,
668 240-250.
669 Soliman, M.F., and Goresy, A.E. (2012) Framboidal and idiomorphic pyrite in the upper
670 Maastrichtian sedimentary rocks at Gabal Oweina, Nile Valley, Egypt: Formation processes,
671 oxidation products and genetic implications to the origin of framboidal pyrite. Geochimica et
672 Cosmochimica Acta, 90, 195-220.
673 Spirakis, C.S. (1996) The roles of organic matter in the formation of uranium deposits in
674 sedimentary rocks. Ore Geology Reviews, 11, 53-69.
675 Steefel, C.I., and Cappellen, P.V. (1990) A new kinetic approach to modeling water-rock interaction:
676 The role of nucleation, precursor, and Ostwald ripening. Geochimica et Cosmochimica Acta,
677 54, 2657-2677.
678 Sun, G.F., Liu, J.P., Liu, K.Q., and Yuan, W.G. (1985) Evolution of a major Mesozoic continental
679 basin within Huabei plate and its geodynamic setting. Oil & Gas Geology, 6, 280-288 (in
680 Chinese with English abstract).

681 Sun, G.F., Xie, Q.Y., Liu, J.P., Xie, S.Y., Liu, K.Q., and Yuan, W.G. (1986) Evolution stacking and
682 hydrocarbon potential of the Ordos Basin - Prototypel analysis of a huge basin in Chinese
683 continental plate. Oil & Gas Geology, 7, 356-367 (in Chinese with English abstract).
684 Sun, L.X., Zhang, Y., Zhang, T.F., Cheng, Y.H., Li, Y.F., Ma, H.L., Yang, C., Guo, J.C., Lu, C., and
685 Zhou, X.G. (2017) Jurassic sporopollen of Yan'an Formation and Zhiluo Formation in the
686 northeastern Ordos Basin, Inner Mongolia, and its paleoclimatic significance. Earth Science
687 Frontiers, 24, 32-51 (in Chinese with English abstract).
688 Turner, C.E., Fishman, N.S., Hatcher, P.G., and Spiker, E.C. (1993) Nature and role of organic
689 matter in sandstone uranium deposits, Grants Uranium Region, New Mexico, USA. Bitumens
690 in Ore Deposits, 9, 239-275.
691 Veblen, D.R., and Ferry, J.M. (1983) A TEM study of the biotite-chlorite reaction and a comparison
692 with petrologic observation. American Mineralogist, 68, 1160-1168.
693 Walker, T.R. (1967) Formation of red beds in modern and ancient deserts. Geological Society of
694 America Bulletin, 78, 353-368.
695 Wang, X.M., Jiao, Y.Q., Wu, L.Q., Rong, H., Wang, X.M., Pan, S.Q., Tang, H., Ji, B., and Song, J.
696 (2011) Major element geochemistry of Jurassic coal in Dongsheng-Shenmu area, Ordos Basin.
697 Acta Sedimentologica Sinica, 29, 520-528 (in Chinese with English abstract).
698 Warren, C.G. (1971) A method for discriminating between biogenic and chemical origins of the
699 ore-stage pyrite in a roll-type uranium deposit. Economic Geology, 66, 919-928.
700 Warren, C.G. (1972) Sulfur isotopes as a clue to the genetic geochemistry of a roll-type uranium

deposit. Economic Geology, 67, 759-767.

White, S.H., Huggett, J.M., and Shaw, H.F. (1985) Electron-optical studies of phyllosilicate intergrowths in sedimentary and metamorphic rocks. Mineralogical Magazine, 49, 413-423.

Xiao, X.J., Li, Z.Y., Fang, X.H., Ou, G.X., Sun, Y., and Chen, A.P. (2004) The evidences and significances of epithermal mineralization fluid in the Dongsheng sandstone type uranium deposit. Bulletin of Mineralogy, Petrology and Geochemistry, 23, 301-304 (in Chinese with English abstract).

Xue, C.J., Chi, G.X., and Xue, W. (2010) Interaction of two fluid systems in the formation of sandstone-hosted uranium deposits in the Ordos Basin: Geochemical evidence and hydrodynamic modeling. Journal of Geochemical Exploration, 106, 226-235.

Yang, H., Fu, S.T., and Wei, X.S. (2004) Geology and exploration of oil and gas in the Ordos Basin. Applied Geophysics, 1, 103-109 (in Chinese with English abstract).

Yang, Y.T., Li, W., and Ma, L. (2005) Tectonic and stratigraphic controls of hydrocarbon systems in the Ordos basin: A multicycle cratonic basin in central China. AAPG Bulletin, 89, 255-269.

Yue, L., Jiao, Y.Q., Wu, L.Q., Rong, H., Xie, H.L., Wang, Q.Y., and Yan, Q.Q. (2019) Selective crystallization and precipitation of authigenic pyrite during diagenesis in uranium reservoir sandbodies in Ordos Basin. Ore Geology Reviews, 107, 532-545.

Yue, L., Jiao, Y.Q., Wu, L.Q., Rong, H., Fayek, M., and Xie, H.L. (2020) Evolution and origins of pyrite in sandstone-type uranium deposits, northern Ordos Basin, north-central China, based on micromorphological and compositional analysis, Ore Geology Reviews, 118, 103334.

721 Zhai, G., Song, J., Jin, J., and Gao, W. (2002) Plate tectonic evolution and its relationship to
722 petroliferous basins: Beijing, Petroleum Industry Press, p. 3-236 (in Chinese).
723 Zhang, C., Yi, C., Dong, Q., Cai, Y.Q., and Liu, H.X. (2018) Geological and geochronological
724 evidence for the effect of Paleogene and Miocene uplift of the Northern Ordos Basin on the
725 formation of the Dongsheng uranium district, China. Journal of Geodynamics, 114, 1-18.
726 Zhang, C., and Liu, H.X. (2019) A growing sandstone type uranium district in South Yili Basin,
727 NW China as a result of extension of Tien Shan Orogen: Evidences from geochronology and
728 hydrology. Gondwana Research, 76, 146-172.
729 Zhang, F., Jiao, Y.Q., Wu, L.Q., Rong, H., and Wang, L.H. (2019a) Relations of uranium
730 enrichment and carbonaceous debris within the Daying uranium deposit, northern Ordos
731 Basin. Journal of Earth Science, 30, 142-157.
732 Zhang, F., Jiao, Y.Q., Wu, L.Q., Rong, H., Li, J.H., and Wan, D. (2019b) Enhancement of organic
733 matter maturation because of radiogenic heat from uranium: A case study from the Ordos
734 Basin in China. AAPG Bulletin, 103, 157-176.
735 Zhang, F., Jiao, Y.Q., Wu, L.Q., Rong, H., and Zang, B. (2020) Changes in physicochemical
736 properties of organic matter by uranium irradiation: A case study from the Ordos Basin in
737 China. Journal of Environmental Radioactivity, 211, 106105.
738 Zhang, H., Bai, Q.Z., Zhang, X.W., and Gao, X.Z. (1995) Formation of the Ordos Basin and its
739 coal-forming tectonic environment. Coal Geology & Exploration, 23, 1-9 (in Chinese with
740 English abstract).

741 Zhang, J.D., Xu, G.Z., Lin, J.R., Peng, Y.B., and Wang, G. (2010) The implication of six kinds of
742 new sandstone-type uranium deposits to uranium resources potential in North China. Geology
743 in China, 37, 1434-1449 (in Chinese with English abstract).
744 Zhang, K., Luo, Z., Zhang, Q., Dai, J., and Yao, H. (1980) Classification of basins and potential
745 hydrocarbons resources in China. Acta Petrolei Sinica, 1, 1-18 (in Chinese with English
746 abstract).
747 Zhang, L., Wu, B.L., Liu, C.Y., Lei, K.Y., Hou, H.Q., Sun, L., Cun, X.N., and Wang, J.Q. (2016)
748 Provenance analysis of the Zhiluo Formation in the sandstone-hosted uranium deposits of the
749 northern Ordos Basin and implications for uranium mineralization. Acta Geologica Sinica,
750 90, 3441-3453 (in Chinese with English abstract).
751 Zhang, L., Liu, C.Y., Fayek, M., Wu, B.L., Lei, K.Y., Cun, X.N., and Li, S. (2017) Hydrothermal
752 mineralization in the sandstone–hosted Hangjinqi uranium deposit, North Ordos Basin, China.
753 Ore Geology Reviews, 80, 103-115.
754 Zhang, L., Liu, C.Y., and Lei, K.Y. (2019) Green altered sandstone related to hydrocarbon
755 migration from the uranium deposits in the northern Ordos Basin, China. Ore Geology
756 Reviews, 109, 482-493.
757 Zhang, L.P., Bai, G.P., Zhao, K.B., and Sun, C.Q. (2006) Restudy of acid-extractable hydrocarbon
758 data from surface geochemical survey in the Yimeng Uplift of the Ordos Basin, China:
759 Improvement of geochemical prospecting for hydrocarbons. Marine and Petroleum Geology,
760 23, 529-542.

761 Zhang, Y.Q., and Liao, C.Z. (2006) Transition of the Late Mesozoic–Cenozoic tectonic regimes
762 and modification of the Ordos basin. Geology in China, 33, 28-40 (in Chinese with English
763 abstract).
764 Zhao, M.W., Behr, H.J., Ahrendt, H., Wemmer, K., Ren, Z.L., and Zhao, Z.Y. (1996) Thermal and
765 tectonic history of the Ordos Basin, China: Evidence from apatite fission track analysis,
766 vitrinite reflectance, and K-Ar dating. AAPG Bulletin, 80, 1110-1134.
767 Zhao, Z.Y. (1990) History of structural evolution, mechanism of formation, and the possible
768 petroliferous area of the Ordos basin. In: Zhao ZY (eds) The formation and evolution of the
769 sedimentary basins and their hydrocarbon occurrence in the north China craton: Xi'an,
770 Northwest University Press, p. 93-102 (in Chinese).
771 Zheng, M.L., Jin, Z.J., Wang, Y., Liu, C.Y., and Xu, G.Z. (2006) Structural characteristics and
772 evolution of north Ordos Basin in late Mesozoic and Cenozoic. Journal of Earth Sciences and
773 Environment, 28, 31-36 (in Chinese with English abstract).
774 Zhu, P.F., Cai, Y.Q., Guo, Q.Y., Liu, W.S., Li, J.H., Zhang, M.L., Qi, F.C., Zhang, Z.L., Jia, L.C.,
775 and Xu, H. (2018) Metallogenetic and geological characterization and resource potential
776 assessment of uranium resources in China. Earth Science Frontiers, 25, 148-158 (in Chinese
777 with English abstract).

778 **Figure captions:**

779 **Figure 1. (a)** Tectonic units of the Ordos Basin showing the location of the Dongsheng U deposit
780 (modified after Deng et al. 2005; Wang et al. 2011); **(b)** A cross section showing the spatial

781 distribution between different colored sandstone units and orebodies in the lower member of the
782 Zhiluo Formation; **(c)** The U-rich sandstones of the Zhiluo Formation in outcrop; **(d)** A map of the
783 different colored sandstone units in the Zhiluo Formation in outcrop; **(e)** The spatial distribution
784 of U contents in the sandstone of the Zhiluo Formation in outcrop.

785 **Figure 2.** Drill holes cross section showing the geochemical zoning in the lower member of the
786 Zhiluo Formation. **(A)** Oxidized zone: a. red sandstone; b. residual red color in green sandstone;
787 c. green sandstone; **(B)** Mineralized zone: d. pyrite and carbonaceous debris in mineralized grey
788 sandstone; e. mineralized grey sandstone; **(C)** Reduced zone: f. mud gravel and carbonaceous
789 debris in barren grey sandstone; g. carbonaceous debris in barren grey sandstone; h. barren grey
790 sandstone. Abbreviations: CD = carbonaceous debris, MG = mud gravel, Py = pyrite.

791 **Figure 3.** Fe^{3+}/Fe^{2+} vs. S_{total}/S^{2-} (**a**), TOC vs. S^{2-} (**b**) and ΔEh vs. pH (**c**) diagrams for different
792 colored sandstones.

793 **Figure 4.** Photographs showing occurrences of Fe-bearing minerals. **(a)** Limonite occurring as
794 rims around pyrite grains in grey sandstone due to being exposed to air; **(b)** Hematite and limonite
795 in red sandstone; **(c)** Disseminated hematite in red sandstone; **(d)** Pyrite grains were oxidized to
796 limonite in yellow sandstone; **(e)** Euhedral hematite grains in red sandstone. Abbreviations: CD =
797 carbonaceous debris, Hem = hematite, Lm = limonite, Py = pyrite.

798 **Figure 5.** Photomicrographs (a, c, i, transmitted light; g, reflected light), back-scattered electron
799 (b, d-f, j-l) and secondary electron (h) images showing occurrences of Fe-bearing minerals. **(a)**
800 Hematite filling pores, sample RD-2; **(b)** Hematite grain; **(c)** Goethite coating K-feldspar, sample

YW-1; **(d)** Goethite grains; **(e)** Framboidal pyrite distributed around the carbonaceous debris; **(f)** Euhedral pyrite; **(g)** Pyrite cement, sample DSC-08; **(h-i)** Chlorite coating the clastic particles; **(j)** Detrital Fe-Ti oxide grains in grey sandstone; **(k)** Altered Fe-Ti oxide; **(l)** Detrital biotite in grey sandstone, sample DSC-20. Abbreviations: Bt = biotite, Cal = calcite, CD = carbonaceous debris, Chl = chlorite, Gth = goethite, Hem = hematite, Kfs = K-feldspar, Kln = kaolinite, Py = pyrite, Qz = quartz.

Figure 6. Back-scattered electron images (a-c, f-j, l) and photomicrographs (d-e, transmitted light; k, reflected light) showing paragenetic relationships of different Fe-bearing minerals. **(a)** Euhedral pyrite along cleavage planes of biotite in grey sandstone; **(b)** Hematite along cleavage planes of biotite in red sandstone; **(c-d)** Goethite along cleavage planes of biotite in yellow sandstone; **(e)** Biotite grains partly altered to chlorite in green sandstone, sample GN-1; **(f)** Biotite partly altered to chlorite filled with hematite and pyrite; **(g)** Pyrite distributed in the matrix of chlorite; **(h)** Pyrite filling in microfractures of altered Fe-Ti oxide; **(i)** Framboidal pyrite distributed near the Fe-Ti oxide; **(j)** Framboidal hematite in red sandstone; **(k-l)** Goethite occurring as rims of pyrite cores. Abbreviations: Bt = biotite; Cal = calcite, Chl = chlorite, Gth = goethite, Hem = hematite, Py = pyrite, Qz = quartz.

Figure 7. Paragenetic sequence of Fe-bearing and U-bearing minerals in the Dongsheng deposit.

Figure 8. Sulfur isotopes of different generations of pyrite. Abbreviations: Pyrite (1) = framboidal pyrite, Pyrite (2) = euhedral + cement pyrite.

Figure 9. Back-scattered electron images showing the relationship between U-bearing and Fe-

bearing minerals. **(a-c)** Coffinite filling in framboidal pyrite; **(d)** Uraninite distributed around the euhedral pyrite grains; **(e)** Coffinite distributed near the euhedral pyrite; **(f)** Coffinite formed around the pyrite cement; **(g)** Coffinite distributed around the pyrite cement replacing Fe-Ti oxide; **(h)** Coffinite precipitates near the Fe-Ti oxide; **(i)** Pyrite replaced by coffinite along cleavage planes in biotite. Abbreviations: Bt = biotite, Cal = calcite, CD = carbonaceous debris, Py = pyrite, Qz = quartz, Urn = uraninite.

Figure 10. Genetic model for different generations of ore-stage pyrite in the Dongsheng U deposit. Abbreviations: BSR = bacterial sulfate reduction, CD = carbonaceous debris, CP = clastic particles, C-Py = cement pyrite, E-Py = euhedral pyrite, F-Py = framboidal pyrite, SRB = sulfate-reducing bacteria.

Figure 1

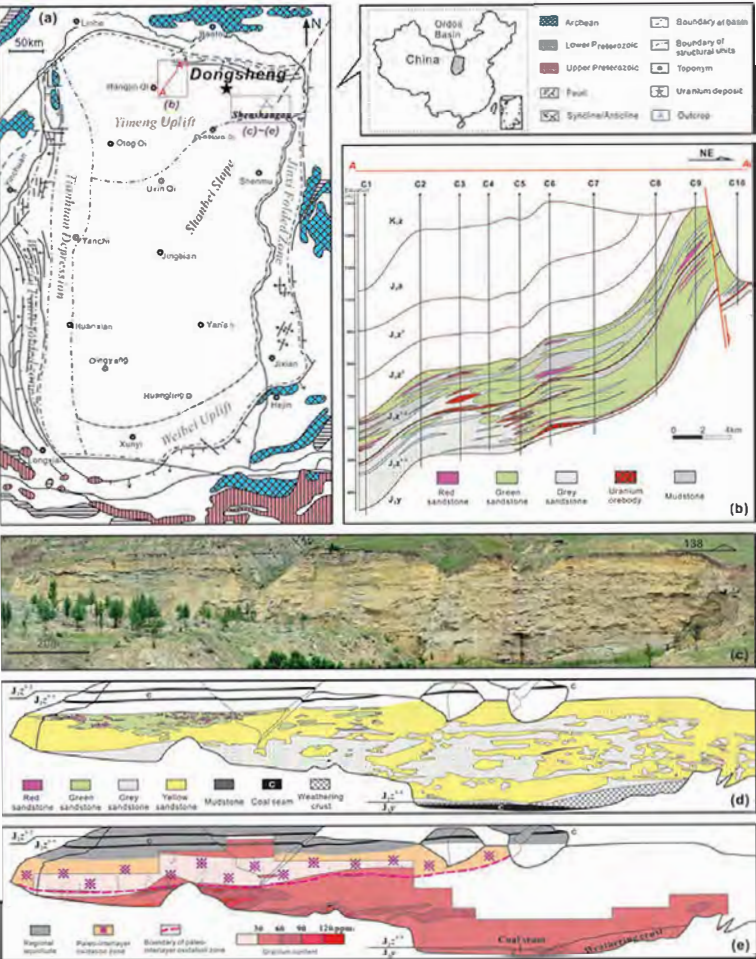
(a)
50km
N
Dongsheng
Yimeng Uplift
Shuntaozhuang
(b)
(c)~(e)
Otog Qi
Uxin Qi
Shenmu
Yanchi
Jingbian
Yan'a
Huanxian
Qingcheng
Huangling
Hejin
Xunyi
Weibei Uplift
Tianhuan Depression
Shanbei Slope
Jinxi Fold Belt
Ordos Basin
China
Archean
Lower Proterozoic
Upper Proterozoic
Fault
Syncline/Anticline
Boundary of basin
Boundary of structural units
Toponym
Uranium deposit
Outcrop
NE
C1
C2
C3
C4
C5
C6
C7
C8
C9
C10
K1z
J2x
J2x1
J2x2
J2x3
J2x4-5
J2y
Red sandstone
Green sandstone
Grey sandstone
Uranium orebody
Mudstone
(b)
138
(c)
Red sandstone
Green sandstone
Grey sandstone
Yellow sandstone
Mudstone
Coal seam
Weathering crust
(d)
Coal seam
(e)

Figure 2

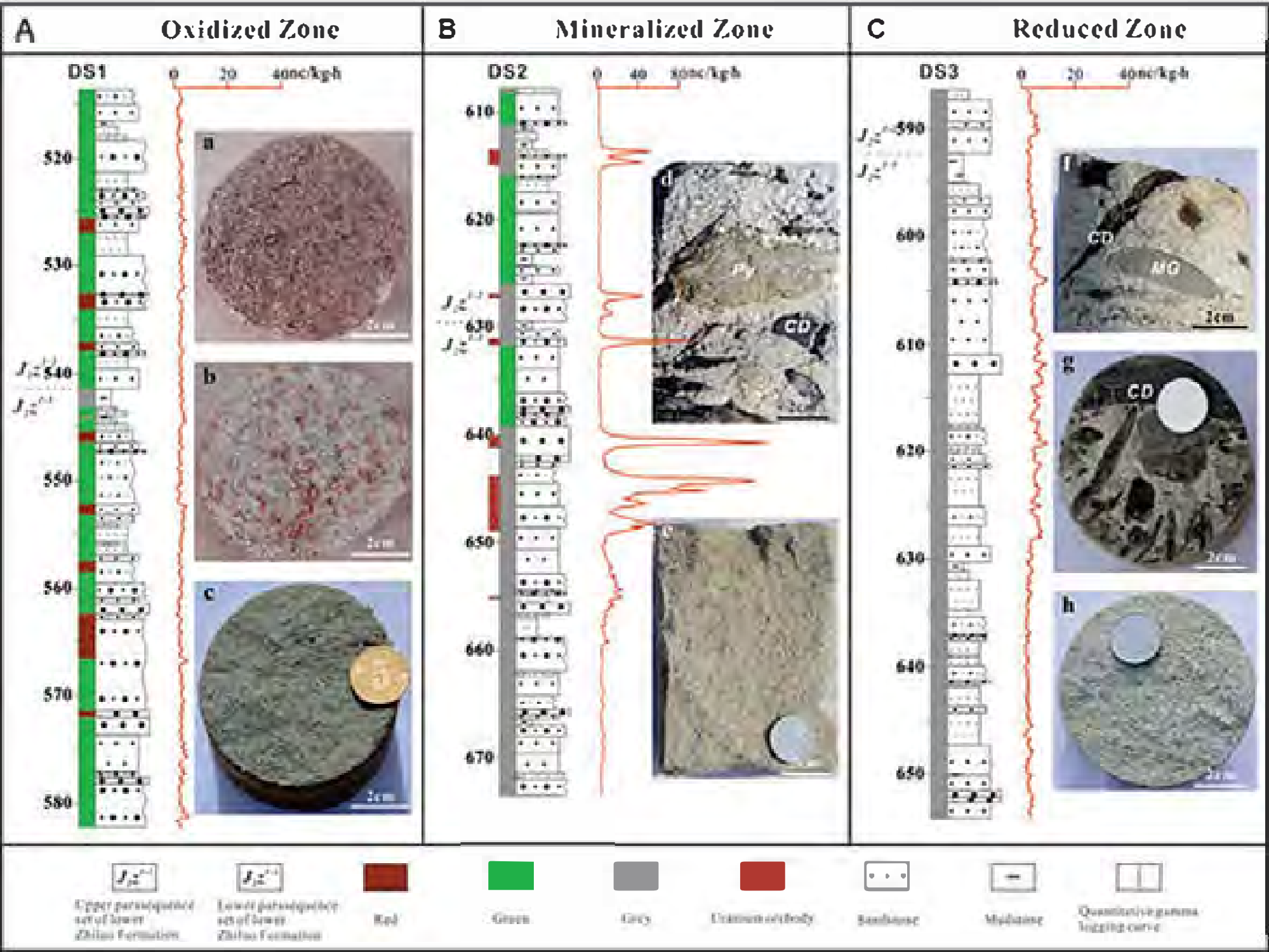
A
Oxidized Zone
B
Mineralized Zone
C
Reduced Zone
DS1
DS2
DS3
0
20
40nc/kgh
520
530
540
550
560
570
580
610
620
630
640
650
660
670
590
600
610
620
630
640
650
a
b
c
d
e
f
g
h
Py
CD
MG
2cm

Figure 3

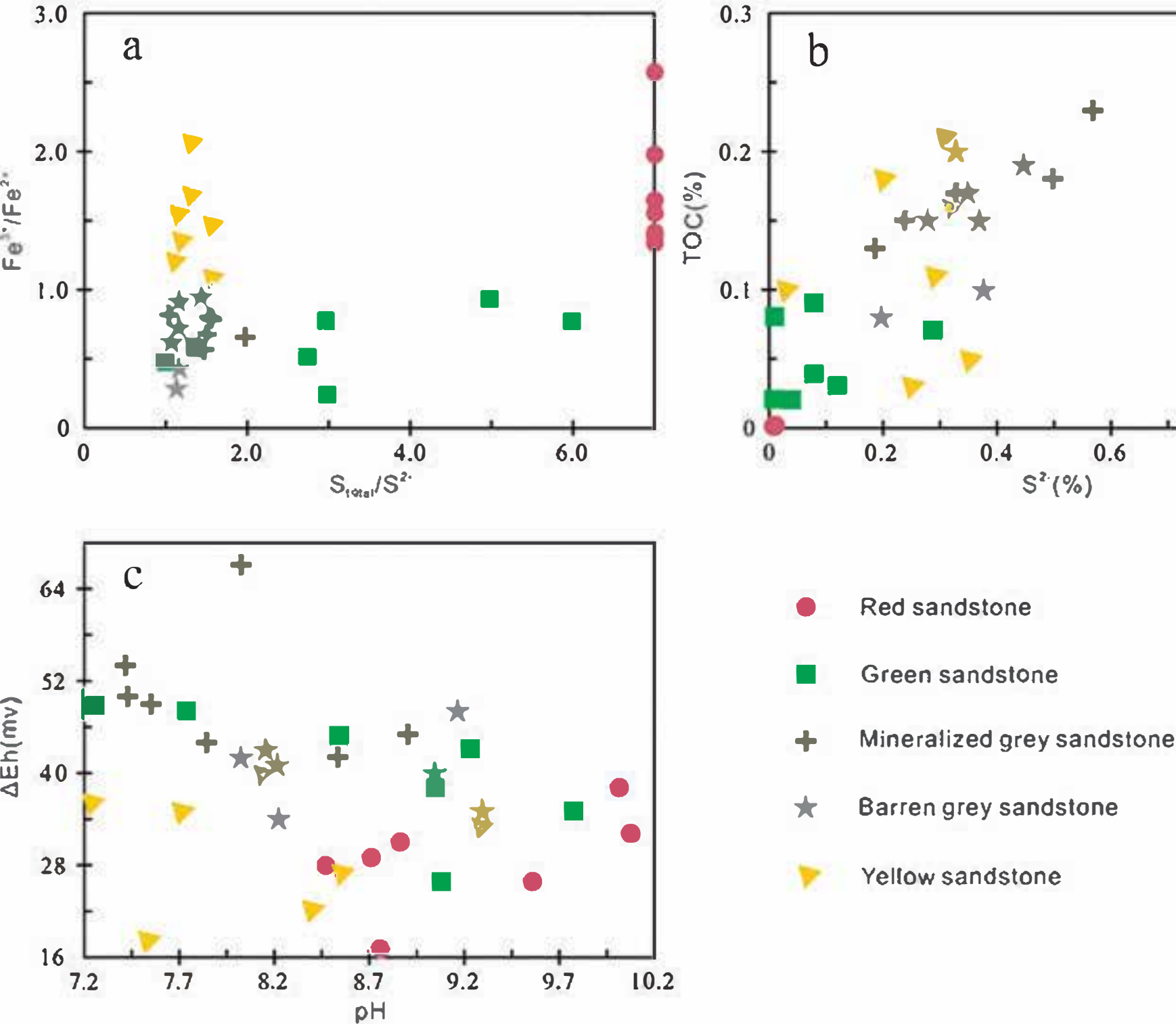
a
b
c
3.0
2.0
1.0
0
0
2.0
4.0
6.0
Fe^{3+}/Fe^{2+}
S_{total}/S^{2-}
0.3
0.2
0.1
0
0
0.2
0.4
0.6
0.8
1.0
TOC(%)
S^{2-}(%)
64
52
40
28
16
7.2
7.7
8.2
8.7
9.2
9.7
10.2
ΔEh(mv)
pH
Red sandstone
Green sandstone
Mineralized grey sandstone
Barren grey sandstone
Yellow sandstone

Figure 4

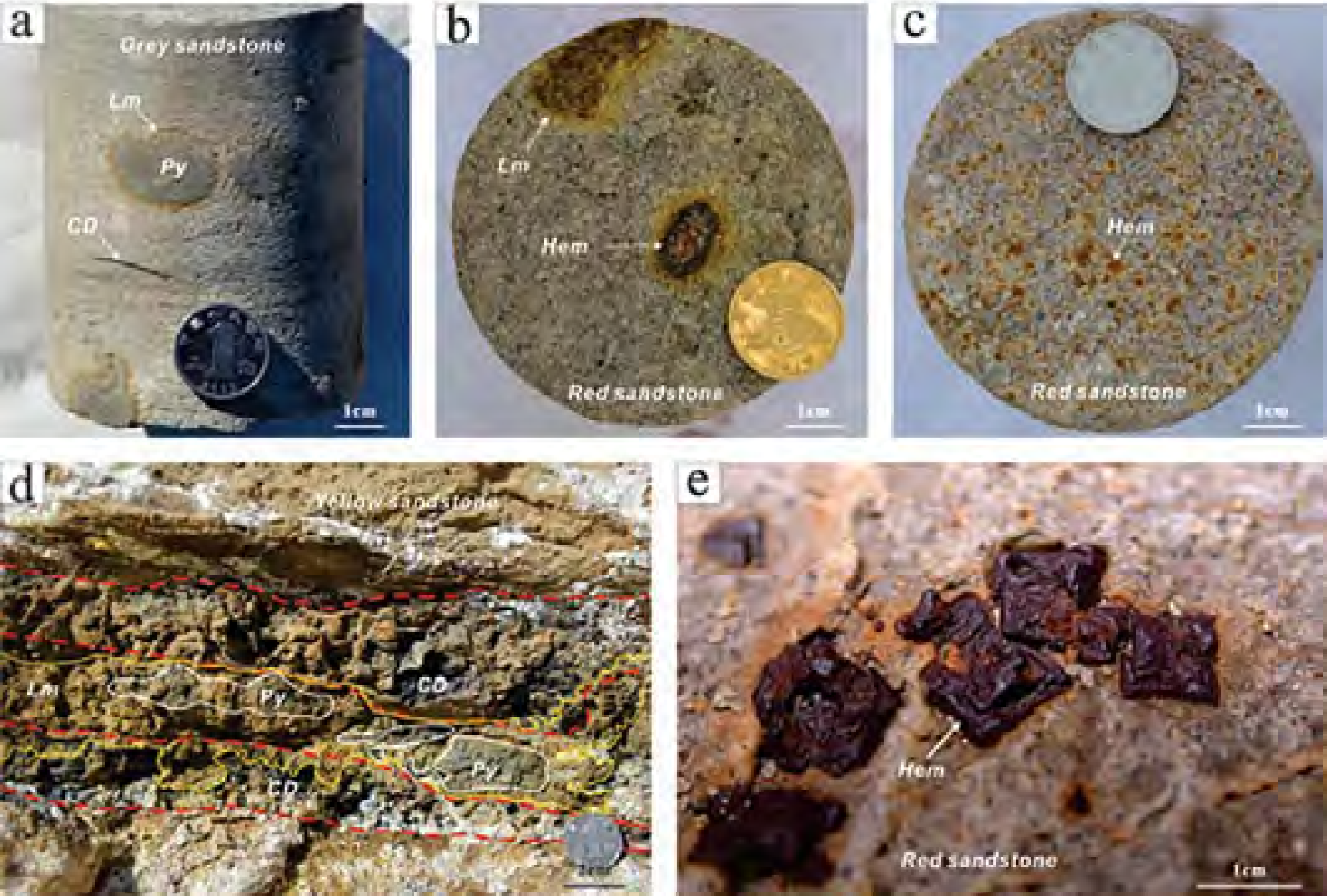
a
Grey sandstone
Lm
Py
CD
1cm
b
Lm
Hem
Red sandstone
1cm
c
Hem
Red sandstone
1cm
d
Yellow sandstone
Lm
Py
CD
Py
CD
e
Hem
Red sandstone
1cm

Figure 5

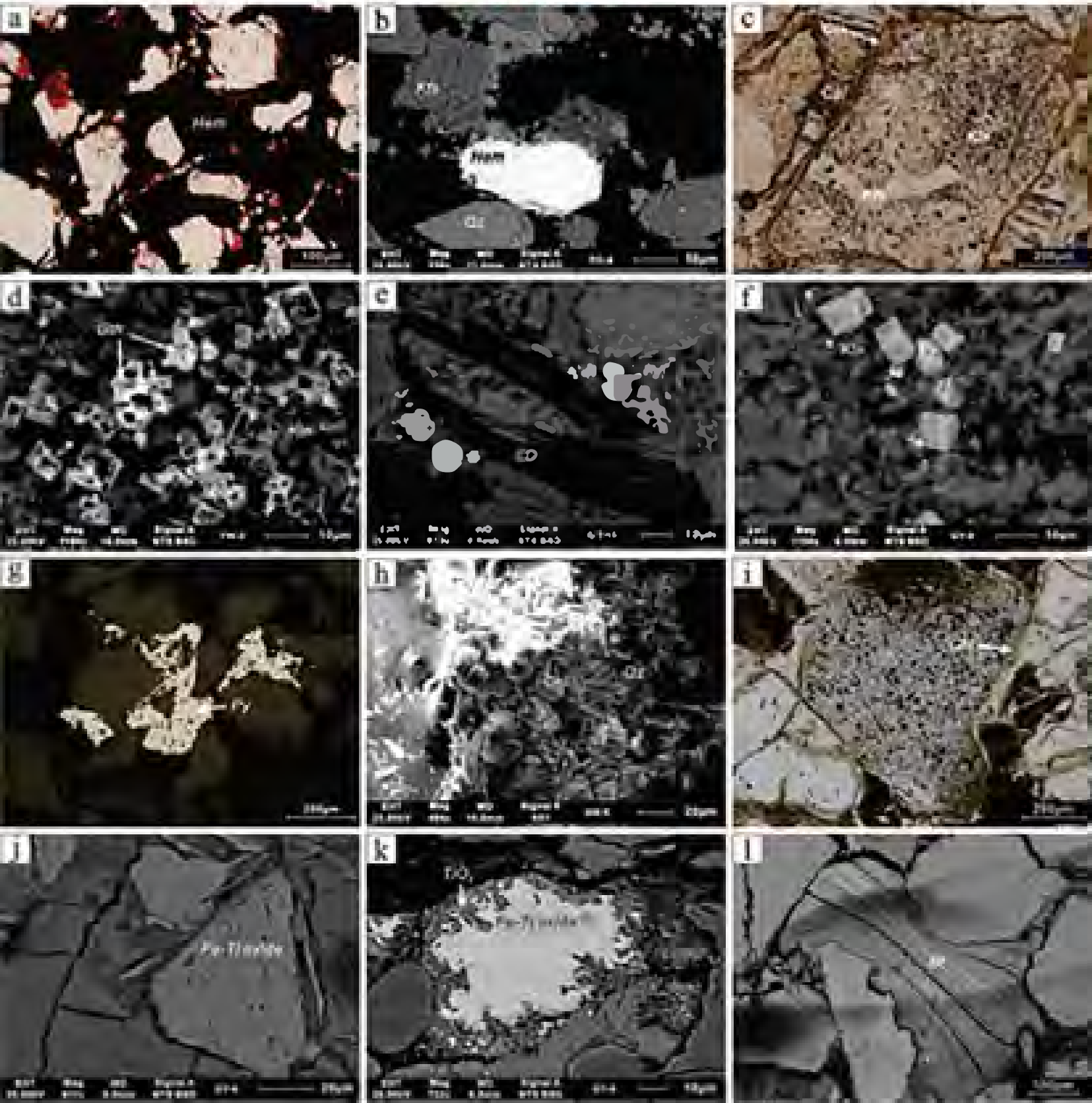

Figure 6

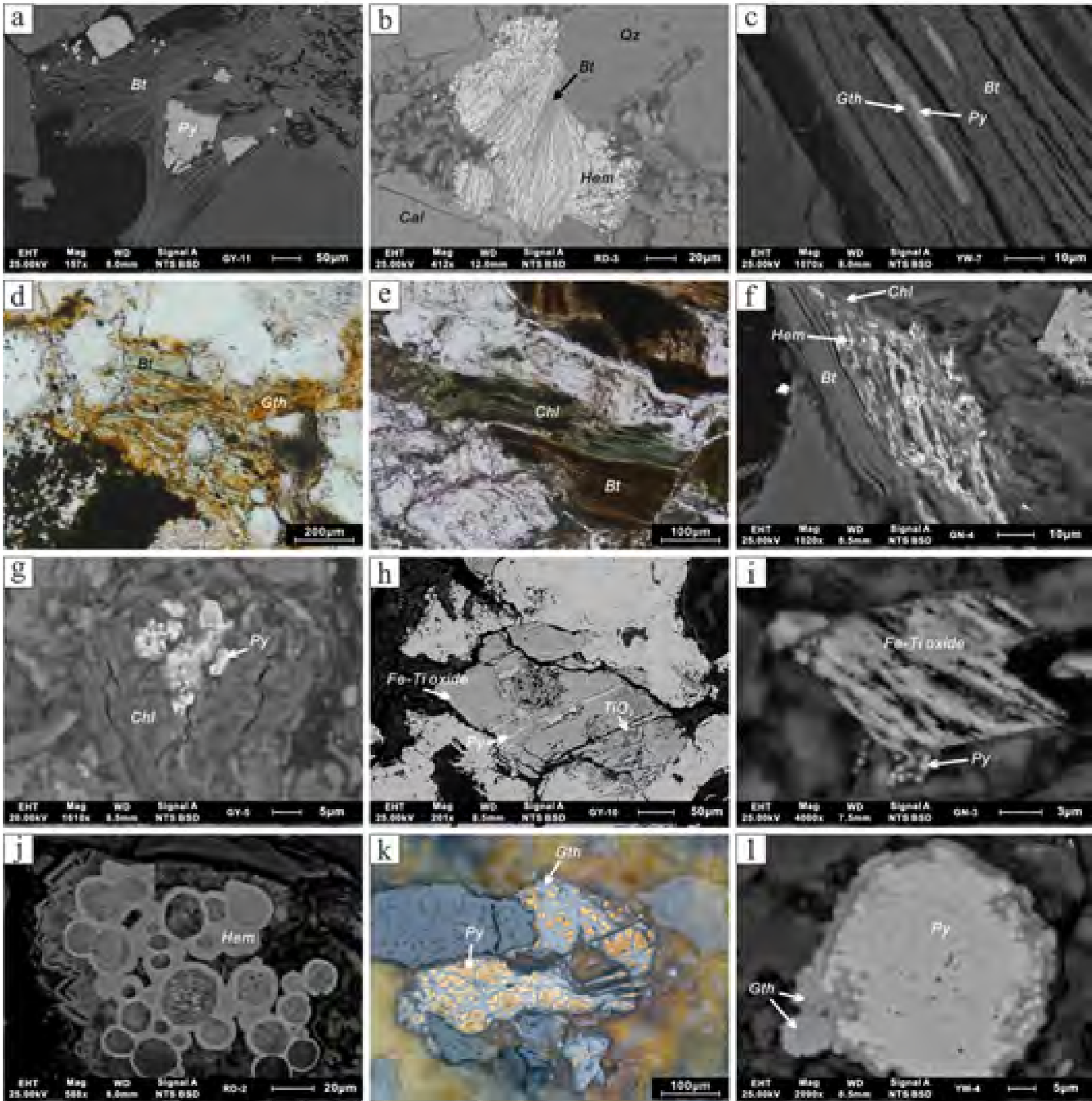
a
Bt
Py
b
Qz
Bt
Hem
Cal
c
Gth
Bt
Py
d
Bt
Gth
e
Chl
Bt
f
Chl
Hem
Bt
g
Py
Chl
h
Fe-Ti oxide
TiO2
i
Fe-Ti oxide
Py
j
Hem
k
Gth
Py
l
Py
Gth

Figure 7

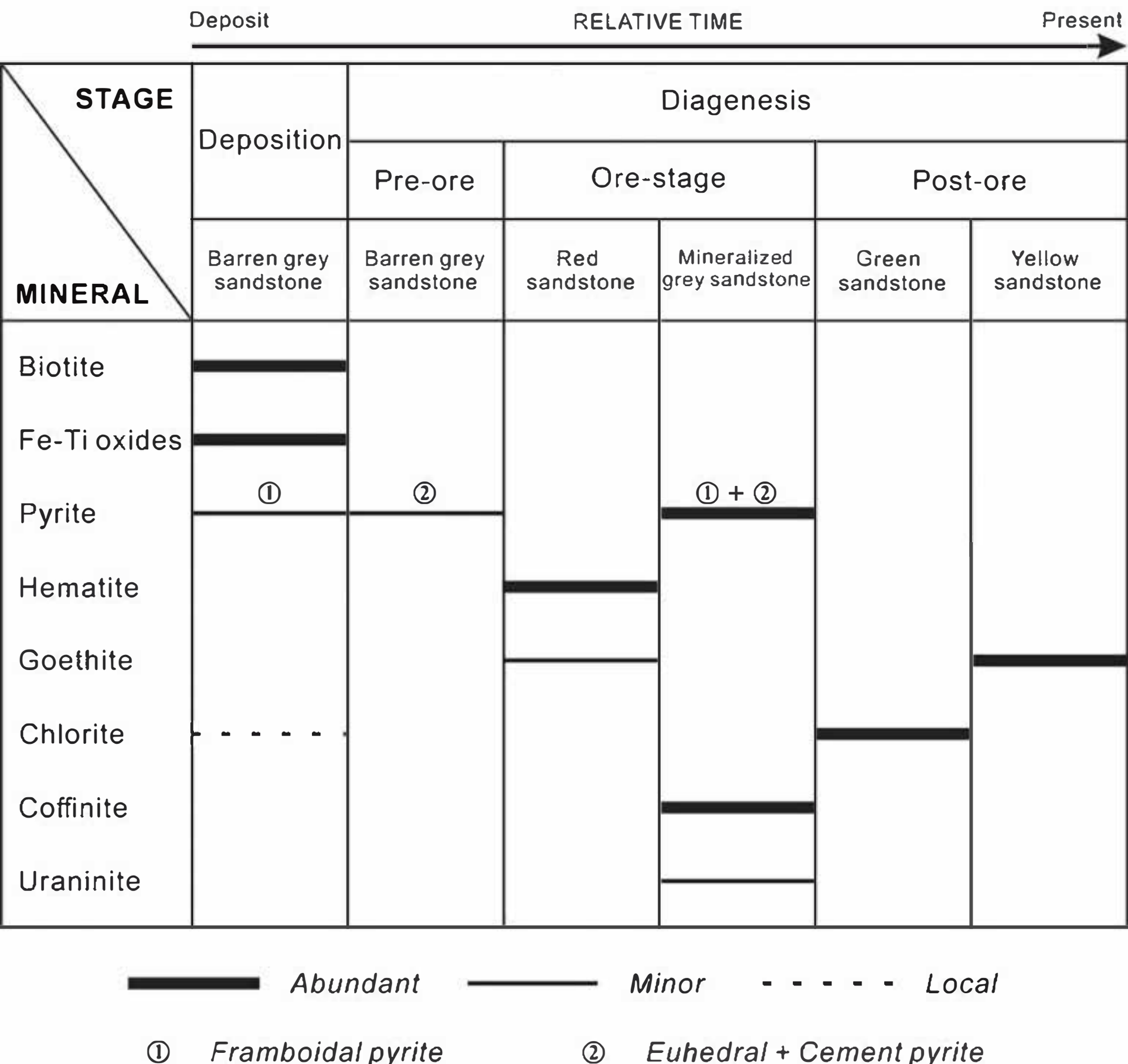
Deposit
RELATIVE TIME
Present
STAGE
MINERAL
Deposition
Diagenesis
Pre-ore
Ore-stage
Post-ore
Barren grey sandstone
Barren grey sandstone
Red sandstone
Mineralized grey sandstone
Green sandstone
Yellow sandstone
Biotite
Fe-Ti oxides
Pyrite
Hematite
Goethite
Chlorite
Coffinite
Uraninite
①
②
① + ②
Abundant
Minor
Local
① Framboidal pyrite
② Euhedral + Cement pyrite

Figure 8

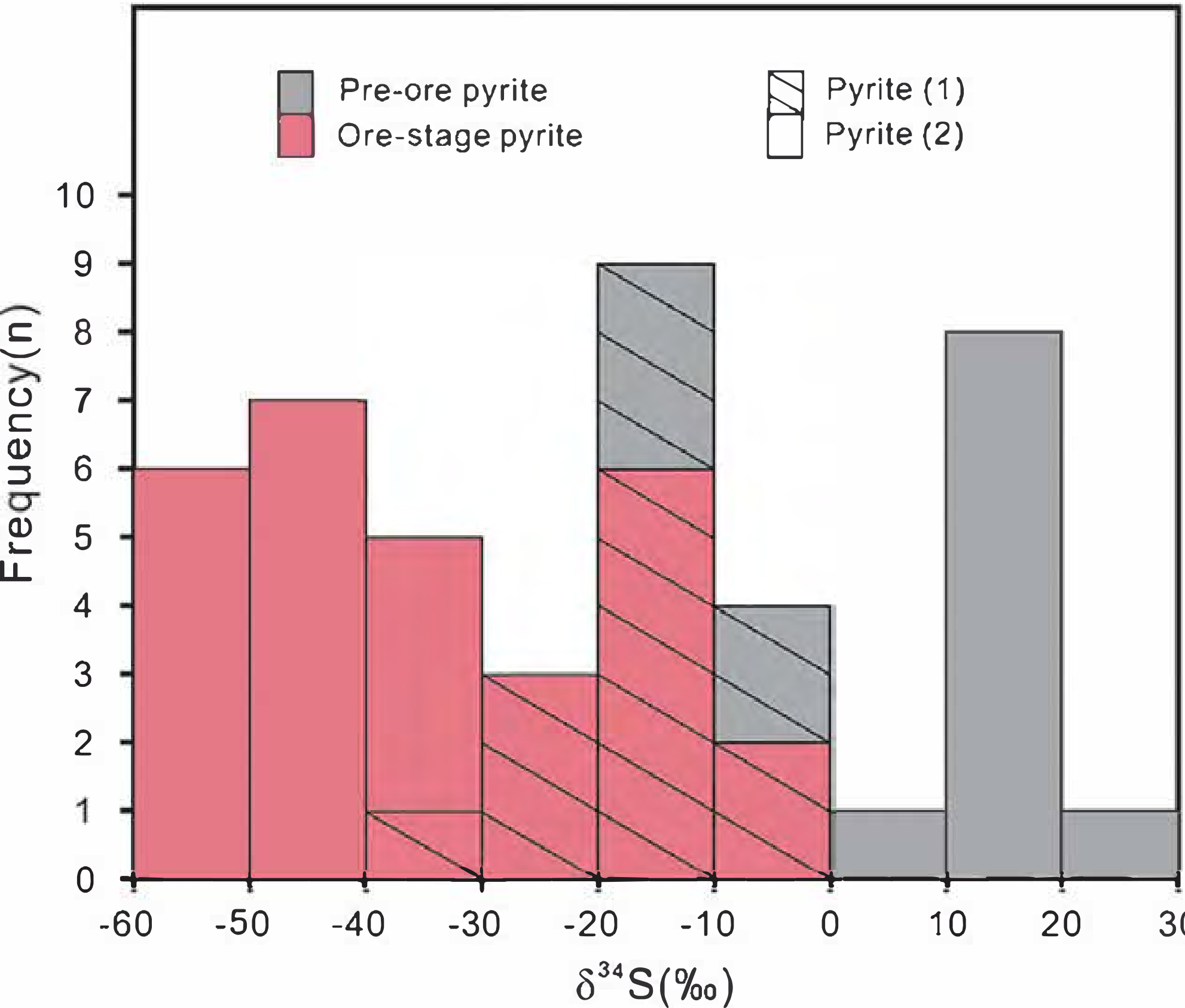
Pre-ore pyrite
Ore-stage pyrite
Pyrite (1)
Pyrite (2)
Frequency(n)
0
1
2
3
4
5
6
7
8
9
10
-60
-50
-40
-30
-20
-10
0
10
20
30
δ34S(‰)

Figure 9

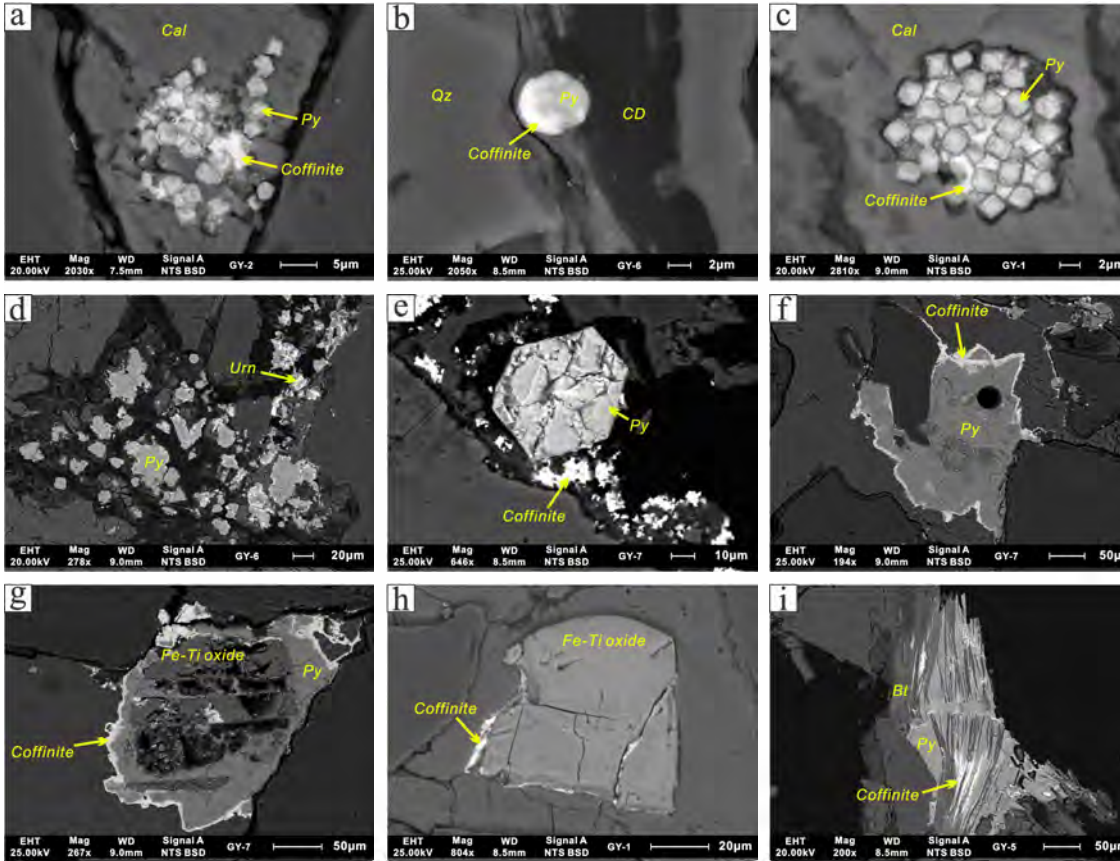
a
Cal
Py
Coffinite
EHT 20.00kV Mag 2030x WD 7.5mm Signal A NTS BSD GY-2 5μm
b
Qz
Py
CD
Coffinite
EHT 25.00kV Mag 2050x WD 8.5mm Signal A NTS BSD GY-6 2μm
c
Cal
Py
Coffinite
EHT 20.00kV Mag 2810x WD 9.0mm Signal A NTS BSD GY-1 2μm
d
Urn
Py
EHT 20.00kV Mag 278x WD 9.0mm Signal A NTS BSD GY-6 20μm
e
Py
Coffinite
EHT 25.00kV Mag 646x WD 8.5mm Signal A NTS BSD GY-7 10μm
f
Coffinite
Py
EHT 25.00kV Mag 194x WD 9.0mm Signal A NTS BSD GY-7 50μm
g
Fe-Ti oxide
Py
Coffinite
EHT 25.00kV Mag 267x WD 9.0mm Signal A NTS BSD GY-7 50μm
h
Fe-Ti oxide
Coffinite
EHT 25.00kV Mag 804x WD 8.5mm Signal A NTS BSD GY-1 20μm
i
Bt
Py
Coffinite
EHT 20.00kV Mag 200x WD 8.5mm Signal A NTS BSD GY-5 50μm

Figure 10

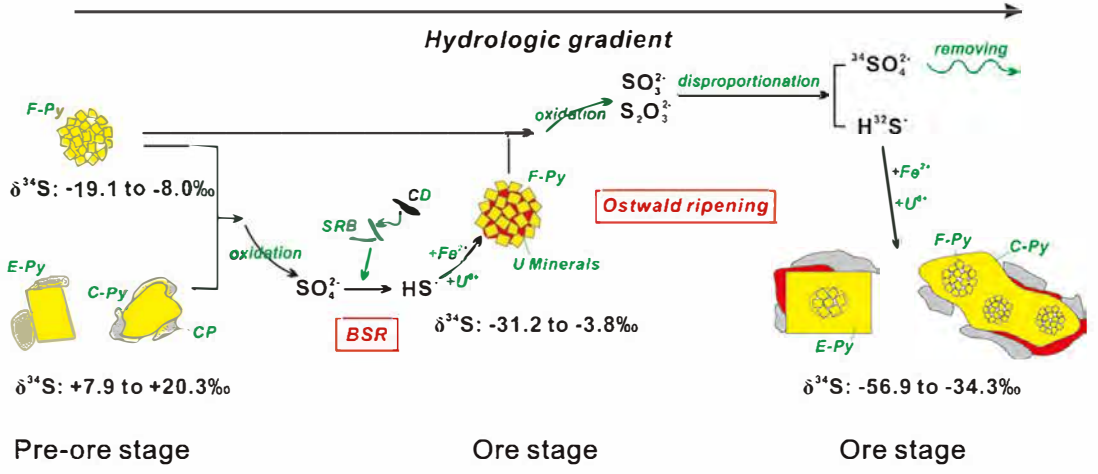
Hydrologic gradient
F-Py
δ34S: -19.1 to -8.0‰
E-Py
C-Py
CP
δ34S: +7.9 to +20.3‰
oxidation
SRB
CD
SO42-
HS-
+Fe2+
+U6+
BSR
F-Py
U Minerals
δ34S: -31.2 to -3.8‰
oxidation
SO32-
S2O32-
disproportionation
34SO42-
H32S-
removing
Ostwald ripening
+Fe2+
+U6+
F-Py
C-Py
E-Py
δ34S: -56.9 to -34.3‰
Pre-ore stage
Ore stage
Ore stage